https://rbgeomorfologia.org.br/
ISSN 2236-5664

Revista Brasileira de Geomorfologia

v. 26, nº 1 (2025)

http://dx.doi.org/10.20502/rbgeomorfologia.v26i1.2583

REVISTA BRASILEIRA DE GEOMORFOLOGIA

Research Article

Geomorphology of Pereiro Massif, Northeast Brazil

Geomorfologia do Maciço do Pereiro, Nordeste do Brasil

Edmundo Rodrigues de Brito[1], Frederico de Holanda Bastos[2], Vanda Carneiro de Claudino Sales[3], Abner Monteiro Nunes Cordeiro[4], Lionel Siame[5]

[1] State University of Ceará, Graduate Program in Geography, Fortaleza, Ceará, Brazil. edmundorodriguez86@gmail.com
ORCID: https://orcid.org/0000-0002-4491-7799
[2] State University of Ceará, Graduate Program in Geography, Fortaleza, Ceará, Brazil. Productivity Researcher 2 (CNPq). fred.holanda@uece.br
ORCID: https://orcid.org/0000-0002-4330-7198
[3] Federal University of Pelotas, Pelotas, Rio Grande Sul, Brazil. vcs@ufc.br.
ORCID: https://orcid.org/0000-0002-9252-0729
[4] Federal University of Rio Grande do Norte, Department of Geography, Center for Higher Education of Seridó, Caicó, Brazil. abner.cordeiro@ufrn.br
ORCID: https://orcid.org/0000-0002-4867-7083
[5] Aix Marseille University, CNRS, IRD, INRAE, CEREGE, Aix-en-Provence, France. siame@cerege.fr.
ORCID: https://orcid.org/0000-0002-4288-9528

Received: 08/05/2024; Accepted: 31/01/2025; Published: 13/02/2025

Abstract: The Pereiro Massif (Northeast Brazil) is a granite relief situated between the Jaguaribe and Portalegre shear zones, exhibiting strong structural control over its morphology. This study aims to analyze the morphostructural context of the massif and interpret its evolution based on denudation rates, using in situ cosmogenic isotope (^{10}Be) production, OSL dating of colluvial deposits, and GIS-based morphometric analyses. The results suggest that the massif represents a relief inherited from a lithostructural framework associated with the Brazilian orogeny, with Cretaceous reactivations and Cenozoic denudational cycles. Its formation is primarily attributed to differential erosion, driven by the greater resistance of granitoids compared to the surrounding metamorphic lithologies. There is no clear evidence of neotectonic activity influencing regional morphogenesis. Denudation rates range from 10.1 to 24.6 m·My^{-1}, indicating higher denudation trends influenced by lithostructural and topographic controls. Post-Miocene morphodynamics were shaped by the regional semi-arid climate, punctuated by humid paleoclimatic variations that account for colluviation between the Last Glacial Maximum (LGM) and the Younger Dryas.

Keywords: Differential erosion; Brazilian Semiarid; Granitic Massif; Cosmogenic Nuclides.

Resumo: O Maciço do Pereiro (Nordeste do Brasil) constitui um relevo granítico situado entre as zonas de cisalhamento de Jaguaribe e Portalegre, com forte controle estrutural na sua morfologia. O trabalho visa analisar o contexto morfoestrutural do maciço e interpretar a sua evolução a partir das taxas de denudação pela produção de isótopos cosmogênicos (^{10}Be) in situ, análise da idade de depósitos coluviais por LOE e uso de SIG para análises morfométricas. Os resultados sugerem o maciço como um relevo herdado de um contexto litoestrutural da orogênese Brasiliana, com reativações cretáceas e ciclos denudacionais cenozoicos. Sua gênese está preferencialmente relacionada à erosão diferencial em função da maior resistência dos granitoides em relação às litologias metamórficas circunvizinhas, sem evidências claras de atividade neotectônica na morfogênese regional. As taxas de denudação variaram de 10,1 a 24,6 m·Ma^{-1} indicando tendências de maior denudação condiciona pelo controle litoestrutural e topográfico. A morfodinâmica pós miocênica foi condicionada pelo clima semiárido regional com variações paleoclimáticas úmidas que explicam coluvionamentos entre o LGM e o Younger Dryas.

Palavras-chave: Erosão diferencial; Semiárido Brasileiro; Maciço Granítico; Isótopos Cosmogênicos.

1. Introduction

In the history of geomorphological studies in Brazil, the Pediplanation model stands out as a widely used approach for explaining the evolution of relief in the Brazilian Northeast. This model attributes the development of slopes to lateral retreat, or backwearing, primarily influenced by an arid climate (BIGARELLA; ANDRADE, 1964; AB'SÁBER, 1969). This process results in sculpted and stepped surfaces extending toward valley bottoms (DRESCH, 1957; DEMANGEOT, 1960; BIGARELLA; ANDRADE, 1964; AB'SÁBER, 1969).

Saadi et al. (2005), Peulvast and Claudino Sales (2004), Bezerra and Vita-Finzi (2000), and Bezerra et al. (2008) introduced a morphostructural and morphotectonic approach that incorporated tectonic processes related to the opening of the Atlantic Ocean and the separation of the South African and South American plates. In this perspective, subsequent Cenozoic reactivations were also considered, along with the influence of continental flexure on relief inversion during this period (PEULVAST; CLAUDINO SALES, 2004), indicating a polygenic and complex origin of the morphologies in the Northeastern region (MAIA; BEZERRA, 2020).

Within this framework, the Pereiro Massif (Figure 1) is one of several granitic bodies in the Borborema Province, formed by rocks originating from the Brazilian syn-orogenic plutonism (650 to 540 Ma) that constitutes the Itaporanga Suite (CAVALCANTE, 1999; BRITO NEVES et al., 2016). Located in the northern part of the Borborema Province in Northeast Brazil (Figure 1B), its evolution has been influenced by the ductile shear zones of Portalegre and Jaguaribe, as well as other fault zones reactivated during the Cretaceous and Cenozoic periods (PEULVAST; CLAUDINO SALES, 2004; BEZERRA; VITA-FINZI, 2000). The massif was ultimately exposed by the action of differential denudation (CAVALCANTE, 1999) (Figure 2).

This orogeny, which resulted in significant plutonism (ANGELIN et al., 2006), was affected by the fragmentation of Gondwana, leading to the separation of South America and Africa during the Cretaceous period (MATOS, 2000). Additionally, this region experienced Cenozoic tectonic reactivations (BEZERRA; VITA-FINZI, 2000) that influenced its geomorphic evolution through changes in base levels, resulting in processes of dissection and aggradation (MAIA; BEZERRA, 2020).

Several proposals have attempted to explain the morphogenesis and evolutionary conditions of the Pereiro Massif. Some consider it (along with nearly all granitic massifs of the Borborema Province) as a residual relief exhumed from the pediplanation process (AB'SÁBER, 1969). Others suggest it is a fault scarp inherited from the shoulder of the Potiguar Rift (an intracontinental rift formed during the separation of Pangaea), with its morphogenesis and evolution linked to the Cretaceous period (PEULVAST; CLAUDINO SALES, 2004). Alternatively, recent tectonics have been proposed as responsible for a local uplift that elevated a sedimentary basin identified by Gurgel (2013) as the Merejo Basin, with the massif's morphogenesis and evolution associated with neotectonic processes. Given these differing interpretations, we believe that the use of new analytical methods can contribute to a more comprehensive understanding of the northeastern relief from a regional perspective.

In this context, this study aims to contribute to the interpretation of the geomorphology of the Pereiro Massif, with emphasis on its genesis and morphostructural context, based on the interpretation of crustal denudation rates obtained through the in situ production of cosmogenic isotopes (^{10}Be), burial dating of colluvium using Optically Stimulated Luminescence (OSL), and morphometric analysis of the drainage network.

2. Study area

Located approximately 400 km from the coast, the Pereiro Massif (Figure 1C) is situated in the northern part of the Borborema Province (Figure 1B) (ALMEIDA et al., 1981), within the central region of the Brazilian tropical semiarid zone (ALVARES et al., 2013) (Figure 1A). It extends across the states of Ceará, Rio Grande do Norte, and Paraíba, with an annual average precipitation of 600 to 800 mm/year (CEARÁ, 2017). The massif exhibits a preferential N-S orientation, measuring 123 km in length and 35 km in width, with elevated areas ranging from 600 to 800 m and a maximum peak at 876 m. It primarily consists of Neoproterozoic granites, granodiorites, and gabbros, with colluvial and alluvial deposits within its territory. The massif is encircled by a lower surface known as the Sertaneja Surface, composed of Archean and Paleoproterozoic metamorphic rocks (PINÉO et al., 2020; CAVALCANTE, 1999). Cretaceous rift basins are also present in the vicinity (GURGEL, 2013).

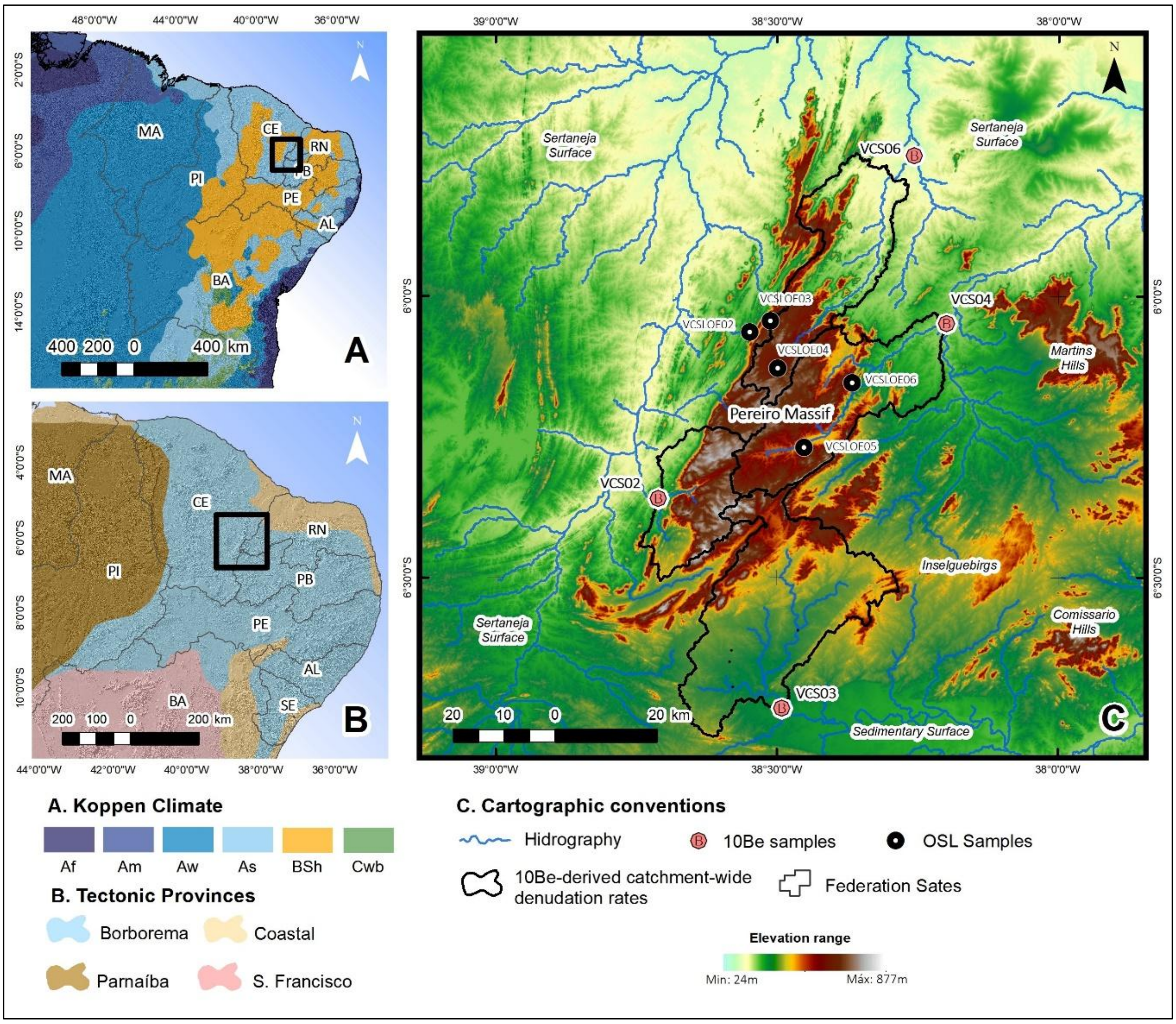

Figure 1. A. Climate context in Northeast of Brazil, classified by Alvarez et. Al (2013): Af- Tropical Zone without dry season; Af – Tropical zone without dry season; Am – Tropical monsoon zone; Aw – Tropical zone with dry winter; As – Tropical zone with dry summer; Bsh – Semi-arid (low latitude/altitude); Cwb – Humid subtropical zone (dry winter, temperate summer). **B.** Geological provinces of Northeast Brazil – Almeida et al. (1981), IBGE (2015), and DEM from FABDEM (HAWKER et al., 2022). **C.** Pereiro Massif (center), with river basins, ^{10}Be and OSL sample locations, and elevation gradient using DEM from FABDEM (HAWKER et al., 2022). Hydrography from IBGE (2015).

In the western sector of the massif, an escarpment marks the interface with the Sertaneja Surface, associated with the Jaguaribe Shear Zone, where rocky pediments dominate the escarpment base. To the east (Figure 1C), the topography transitions gradually over 19.5 km (elevation drop of ~400 m), characterized by steep ramps, knickpoints, and dissected steps influenced by varying lithotypes. To the north and south, topographic variation is linked to faults and fractures, which have shaped ridges, peaks, and associated pediments (elevations: 200–650 m), underscoring the interplay between geological structure and topography.

The lithology of the Pereiro Massif originated during the Ediacaran (≈650–540 Ma) syn-orogenic plutonic event that formed the Itaporanga Suite, a major magmatic episode of the Brazilian Orogeny within the Borborema Province (GOMES; VASCONCELOS, 2000). This orogeny produced extensive plutonic bodies across Northeast Brazil (ANGELIN et al., 2006) and is linked to the Estaterian (≈1.8–1.6 Ga) and Riacian (≈2.3–2.05 Ga) suites of the Serra do Deserto Suite, Jaguaretama Complex, and Caicó Complex (ALMEIDA et al., 1981; NASCIMENTO; MEDEIROS; GALINDO, 2015). These complexes form the metamorphic basement and host enclaves of diverse lithotypes (Figure 2).

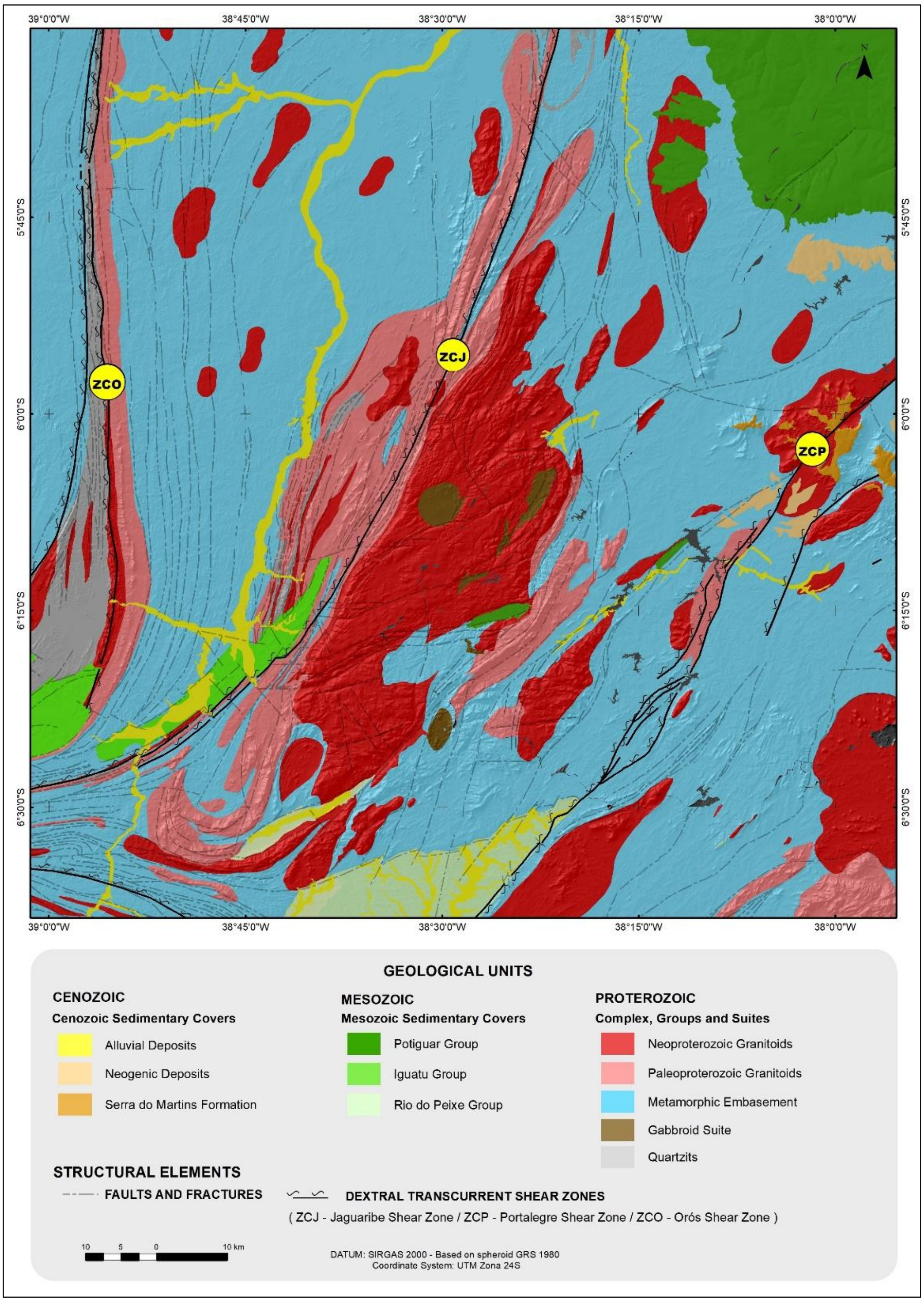

Figure 2. Geological context of the Pereiro Massif. DEM from FABDEM (HAWKER et al., 2022); geologic features (units and structural elements) from CPRM (2020) and IBGE (Jaguaribe SB.24-Z and Souza SB.24-Z-A sheets, 2020).

In its geomorphological evolution, the Pereiro Massif can be interpreted as a fault scarp potentially inherited from the shoulder of the Potiguar Rift, which formed during the breakup of Pangaea (PEULVAST; CLAUDINO-SALES, 2004). This process generated a series of intracontinental rifts, including the Potiguar and Araripe shoulders, among smaller structures (CASTRO; BEZERRA, 2015). The massif exhibits a linear NE-SW trend, likely reflecting structural control inherited from the Jaguaribe dextral transcurrent shear zone, which borders its steep western face (FRANÇOLIN; SZATMARI, 1987).

The Neoproterozoic granitic pluton of the Itaporanga Suite constitutes approximately 82% of the Pereiro Massif's total area, forming its most prominent geological feature. Embedded within it are gabbroid suites, alluvial and colluvial deposits, and depositional surfaces (Figure 3), creating a composite body with distinct granulometric variations (CAVALCANTE, 1999).

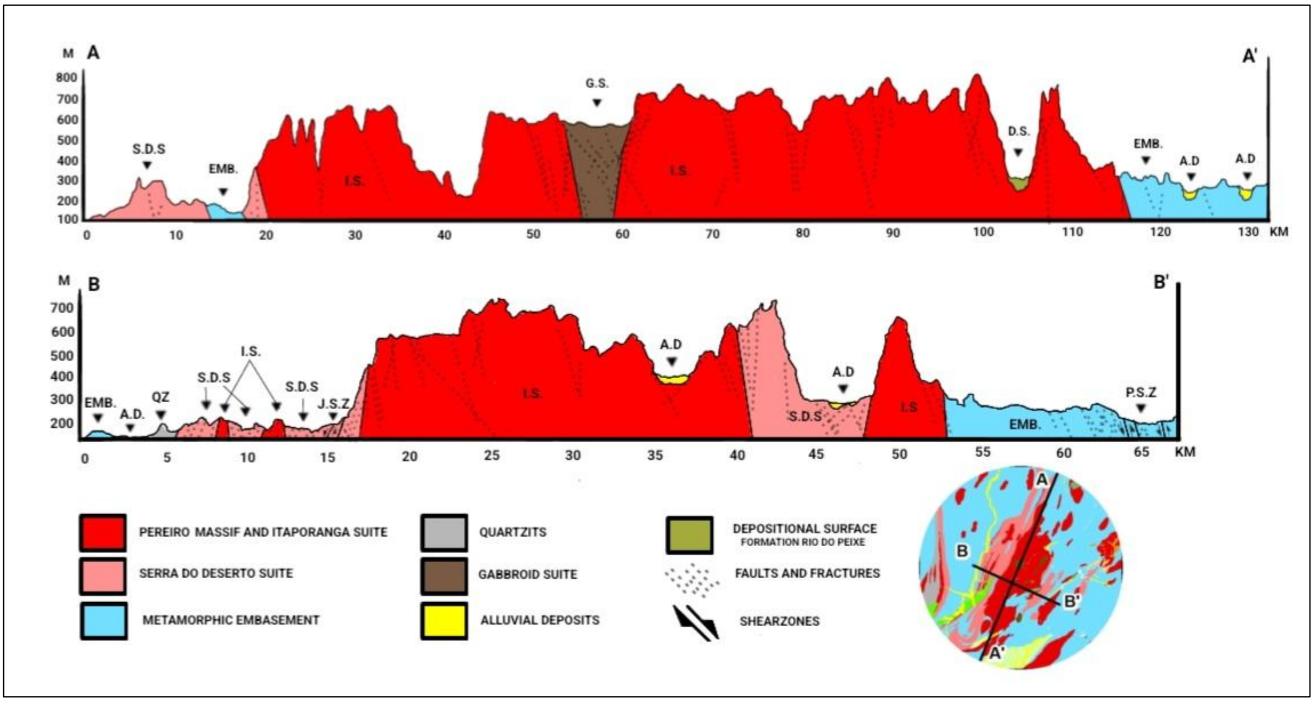

Figure 3. Geological profiles of Pereiro Massif. Abbreviations: S.D.S. – Serra do Deserto Suite: augen gneiss, granite, diorite; A.D. – Alluvial Deposits: sands, silts; EMB – Metamorphic Basement; QZ – Quartzites; I.S. – Itaporanga Suite: biotite, feldspars (various sizes), porphyritic granites, monzogranites; G.S. – Gabbroid Suite: gabbros, granites; D.S. – Depositional Surface: Mesozoic sandstones, limestones; J.S.Z. – Jaguaribe Shear Zone; P.S.Z. – Portalegre Shear Zone.

The massif's composition includes granites, diorites, granodiorites, and monzonites, predominantly with coarse-grained and porphyritic feldspars. It exhibits subparallel to parallel magmatic foliation relative to internal gneisses and mylonitic foliation near bordering shear zones (PINÉO et al., 2020). Intrusions of intermediate plutonic bodies, such as Dom Severiano (north) and Caiçara (Icozinho) (south), surround the massif (CAVALCANTE, 1999).

On the eastern margin, adjacent to the Pereiro core and connected to the Serra do Deserto Suite (Paleoproterozoic granites, gneisses, and augen gneisses), xenolithic and individualized gneissic leucogranites are prominent. These feature quartz, plagioclase, K-feldspar, hornblende, and biotite, with biotite compositions resembling those of the Cangati Granitoid Suite (CAVALCANTE, 1999).

Other lithotypes intruding the Itaporanga/Pereiro Massif, Serra do Deserto Suite, and metamorphic basement include: Dona Inês Intrusive Suite - hornblende-biotite granites and fine- to medium-grained leucogranites (MCMURRY et al., 2015), acting as a divide for Santana Creek (SE portion); Serra de São José Group - quartzites, metavolcanic rocks, marbles, and gneisses (E portion); São João do Sabugi Intrusive Suite - gabbroid compositions (PINÉO et al., 2020; CAVALCANTE, 1999).

Sedimentary formations, such as the Pendências and Antenor Navarro Formations, are notable for their elevation (~320 m) and composition. These occur in the SSW portion of the massif, in contact with the Catingueira Intrusive Suite and the Jaguaretama Complex basement. They comprise arkosic sandstones, polymictic conglomerates, and are overlain by alluvial deposits of the Capim River Formation (Figure 2) (PINÉO et al., 2020).

3. Methodology

3.1. Geomorphological characterization

The geomorphological characterization of the Pereiro Massif was conducted through a combination of fieldwork, literature review, and GIS tools to process data from the FABDEM - COPDEM30 enhanced imagery, which involved the removal of buildings and forests (HAWKER et al., 2022). This process enabled the creation of various products, including a hillshade for enhanced identification of topographic variations, slope maps for gradient assessment, and kernel density analyses to identify structural lineament hotspots. These lineaments were extracted from the images using the PCI Geomatics application and mapped at a 1:150,000 scale.

The integration of analyses derived from geomorphological characterization, erosion rates using in situ-produced ^{10}Be, and OSL dating methods, along with morphometric analysis, was performed using ESRI ArcGIS software. This integration resulted in the generation of additional products, including hydrographic basins, drainage patterns, topographic profiles, and flow direction maps, among others. Collectively, these resources provide a comprehensive and detailed framework for understanding the key factors influencing the evolutionary processes of the Pereiro Massif.

3.2. Cosmogenic Isotopes – ^{10}Be

In situ-produced ^{10}Be is widely used in quartz-rich environments to quantify denudation rates and landscape dynamics over timescales of 10^3–10^6 years, across diverse geomorphic settings (GRANGER et al., 2013; PORTENGA; BIERMAN, 2011; CODILEAN et al., 2018, 2022). In river basins, it effectively links sediment flux to catchment-scale erosion (BROWN et al., 1995; BIERMAN; STEIG, 1996; GRANGER et al., 1996). Basin-wide denudation rates were estimated by measuring ^{10}Be concentrations in riverbed quartz, assuming fluvial sediment represents erosional dynamics across the sampled catchment (VON BLANCKENBURG, 2005, 2014; GRANGER; SCHALLER, 2014).

Converting *in situ*-produced ^{10}Be concentrations into basin-wide erosion rates assumes that the fluvial sediment is representative of the erosional dynamics across the entire sampled catchment (GRANGER et al., 1996). Surface production rates and shielding correction due the surrounding topography were determined using scaling scheme by Stone (2000) and shielding formalism by Dunne (1999), applied for each pixel of digital elevation grids using in-house MATLAB scripts and those from Balco et al. (2008). Stone scaling factors for spallation were derived using a grid of 30 m resolution, while topographic shielding was derived using a grid of 90 m resolution and a 15° step angle. This gridded approach allows spatially integrating topographic shielding and scaling factors for the cosmogenic production due to high energy neutrons (Pn, latitude-elevation dependent; STONE, 2000) as well as fast and stopping muons ($P_{\mu s}$ and $P_{\mu f}$, elevation dependent only; BRAUCHER et al. 2011).

Basin-wide and local erosion rates were calculated, using the following equation:

$$N(D,t) = \frac{P_n}{\lambda + \frac{\rho D}{\Lambda_n}} \cdot \left(1 - e^{-\left(\lambda + \frac{\rho \cdot D}{\Lambda_n}\right)t}\right) + \frac{P_{\mu s}}{\lambda + \frac{\rho \cdot D}{\Lambda_{\mu s}}} \cdot \left(1 - e^{-\left(\lambda + \frac{\rho \cdot D}{\Lambda_{\mu s}}\right)t}\right) + \frac{P_{\mu f}}{\lambda + \frac{\rho \cdot D}{\Lambda_{\mu f}}} \cdot \left(1 - e^{-\left(\lambda + \frac{\rho \cdot D}{\Lambda_{\mu f}}\right)t}\right) \quad (1)$$

where N corresponds to the nuclide concentration as a function of the rate of denudation (D, g cm-2 yr^{-1}), for the case of a steady-state erosion and cosmic ray irradiation after a long time ($t \gg \frac{1}{\lambda + \frac{D\rho}{\Lambda}}$, e.g., LAL, 1991).

In this equation Λ_n, $\Lambda_{\mu s}$, $\Lambda_{\mu f}$ are the effective apparent attenuation lengths of neutrons (160gcm^{-2}), slow muons (1500gcm^{-2}), and fast muons (4320 g·cm^{-2}), respectively (BRAUCHER et al., 2011). λ is the radioactive decay constant of ^{10}Be, and ρ (2.3±0.2 g·cm^{-3}) is the surface material densities. The results are presented in Table 5.

The sampling strategy was designed to analyze small basins with areas of 118.58 km² (VCS02), 1,353.71 km² (VCS03), 719.85 km² (VCS04), and 596.92 km² (VCS06), encompassing the slopes of the Pereiro Massif to interpret erosion evolution trends within the massif and correlate these denudation data with other morphometric and lithostructural parameters.

The chemical preparation of samples was conducted at the Laboratory of Cosmogenic Nuclides at the University of Vermont, Burlington, USA. Initially, mechanical and chemical procedures such as grinding, sieving, and preliminary mineral elimination were performed (CORBETT, BIERMAN & ROOD, 2016). Subsequently, the samples underwent a chemical process involving the removal of meteoric ^{10}Be, the addition of ^{9}Be using a carrier solution prepared at the University of Vermont with a concentration of 304 μg·mL^{-1} (1.673×10^{19} atoms added), complete quartz dissolution, evaporation, precipitation, elimination of metallic cations and anions, and oxidation.

In situ-produced ^{10}Be measurements were carried out at the PRIME Laboratory in California, USA. The samples were normalized to the $^{10}Be/^{9}Be$ ratio using the standard 07KNSTD3110, with an assumed ratio of 2.850×10^{-15} (NISHIIZUMI et al., 2007) and a ^{10}Be half-life of 1.387 ± 0.012 Myr (KORSCHINEK et al., 2010; CHMELEFF et al., 2010). The reported analytical uncertainties (expressed as 1σ) included uncertainties associated with AMS counting statistics, the 0.5% AMS internal error (ARNOLD et al., 2010), and errors measured through the blank sample.

3.3. Optically Stimulated Luminescence – OSL

Optically Stimulated Luminescence (OSL) has been widely applied in geological and geomorphological studies (HUNTLEY et al., 1985, 1996; SAWAKUCHI et al., 2016) due to its ability to estimate burial ages dating back to the Quaternary period. This capability provides a foundation for analyzing erosional processes associated with paleoclimates (LIMA; PEREZ FILHO, 2020; LISTO et al., 2023) and neotectonic activity (GURGEL, 2013; GOUVEIA; SOUZA, 2015).

Five OSL samples were selected (Figures 1 and 11) based on toposequence criteria (DRUMOND et al., 1996) and stratigraphic breaks in colluvial deposits (GURGEL, 2013). Sample locations were identified using FABDEM imagery (HAWKER et al., 2022), cross-referenced with georeferenced geological formation data (PINÉO et al., 2020), and verified for accessibility using ESRI ArcMap. Samples VCSLOE-02 and VCSLOE-03 were collected from the western portion within colluvial deposits at the base of the escarpment; VCSLOE-04 from colluvial deposits overlying the gabbroid suite; and VCSLOE-05 and VCSLOE-06 from colluvial deposits on the sediment surface of the Nazaré River. These samples aimed to assess paleoclimatic influences on colluviation in the Pereiro Massif during the Late Pleistocene.

OSL sample collection followed the technical specifications outlined by Sallum et al. (2007). Aluminum tubes (30 cm long and 10 cm in diameter) were used for sample extraction. The tubes were inserted into the ground after removing 50 cm of surface material to prevent sunlight exposure, ensuring that the in situ luminescence signal remained intact.

Equivalent doses (De) were measured at Datação™ Laboratory (São Paulo, Brazil) using the Single Aliquot Regeneration (SAR) protocol (AITKEN, 1998; MURRAY; WINTLE, 2000; WALKER, 2005). Samples underwent chemical pretreatment to remove organics and carbonates, followed by granulometric separation (100–160 μm fraction). These fractions were exposed to solar radiation and cobalt-60 for calibration. The SAR protocol mitigates grain sensitivity variations by generating multiple aliquot ages (WALLINGA et al., 2000).

Dating employed the Central Age Model (GALBRAITH et al., 1999), with 10 aliquots per sample. Preheat and cut-heat temperatures were set to 200°C and 160°C, respectively. Luminescence signals were integrated over 1–5/240–250 channels (20-second total read time, 250 channels at 12.5 channels/sec). Background subtraction used the last 10 channels (0.8 s) from the initial 0.4 s (5 channels) of signal (AITKEN, 1998; MURRAY; WINTLE, 2000).

Recovery and recycling tests were conducted, with all aliquots yielding values within the SAR analysis standard range of 0.9 to 1.1 (MURRAY; WINTLE, 2000; WALKER, 2005) (Figure 12). Statistical modeling was also performed, where the Equivalent Doses (De) were analyzed using radial and density plots, considering individual uncertainties. The Central Age Model was then used to determine the average age, incorporating dispersion values (GALBRAITH; GREEN, 1990; SILVERMAN, 1990).

Annual dose rates for each sediment sample were calculated by determining the concentration of radioisotopes (thorium, uranium, and potassium) using gamma spectrometry (GUÉRIN et al., 2012). Measurements were obtained with a NaI (Tl) detector (models 802-2 and 727, Canberra Industries Inc.). Conversion factors were applied based on sample parameters, including depth, grain size, water content, and geographic coordinates. The cosmic ray contribution was estimated using the equations of Prescott & Hutton (1994).

3.4. Morphometric Analysis

This study applied morphometric analyses based on geometric parameters (form factor, compaction ratio, circularity index, basin area, and perimeter), topographic parameters (elevation, slope, average *ksn*, total knickpoints), and hydrographic parameters (drainage patterns, magnitude, flow direction, channel length, river elevation range, drainage density). These parameters serve as indicators of structural control and the potential occurrence of recent tectonic activity (TEODORO et al., 2007). All hydrographic and topographic parameters were extracted from DEM FABDEM V1-2. The geometric parameters were calculated based on Tucci (2000), where the Form factor (*Kf*) is defined by the quotient of the area of the basin (*A*) and the length of the main river (*L*).

$$Kf = A / L^2 \tag{2}$$

The Compaction ratio (*Kc*) is defined by the quotient of the perimeter (*P*) of the basin and the square root of its area (*A*) as a function of the constant 0.28.

$$Kc = 0{,}28 * P / \sqrt{A} \tag{3}$$

The Circularity (*Ic*) is characterized by the quotient of the area of the basin (*A*) and the perimeter (*P*) squared as a function of the constant 12.57.

$$Ic{=}12{,}57{*}A/P2 \tag{4}$$

These parameters are fundamental for drainage analysis, particularly when using the Slope vs. Length Index (*SL*), which helps detect anomalies in the longitudinal river profile. This index is a key tool for identifying processes associated with neotectonic activity (HACK, 1973; SILVA et al., 2006).

Since the *SL* index is based on a semi-logarithmic relationship, it assesses slope reductions along river channel sections. The total *SL* index was calculated using the altitude variation (*ΔH*) from the spring to the river mouth, divided by the natural logarithm of the main river length (*L*):

$$SL{=}\Delta H/LogL \tag{5}$$

The *SL* per section was calculated using 2 km intervals along each river. The index was determined by multiplying the total river length (*L*) by the ratio of the elevation difference between the start and end of each interval (*ΔH*) to its length (*ΔL*).

$$SLs = (\Delta H/\Delta L)L \tag{6}$$

The resulting *SL* values typically range from 0 to 2, indicating equilibrium, 2 to 10 for second-order anomalies, and above 10 for first-order anomalies (ETCHEBEHERE, 2006) (Figure 9).

In addition to topographic characteristics, the river geometry – reflecting climatic and tectonic forces, variations in base level and sediment transport, and differences in bedrock erodibility – was also analyzed (SCHWANGHART; SCHERLER, 2017). For this purpose, the *ksn* metric, based on a fixed reference concavity index (θ_{ref}), was employed (KIRBY; WHIPPLE, 2012; WOBUS et al., 2006), and knickpoints were identified using the drainage network extracted from FABDEM V1-2, applying a hydrographic gradient of 1000 and a vertical drop (*dz*) of 30 (PEYERL et al., 2023).

The *ksn* parameter is a channel gradient metric corrected for variations in drainage area (WHIPPLE et al., 2017; WOBUS et al., 2006). High *ksn* values indicate elevated denudation rates, tectonic uplift, or greater rock erodibility, whereas low *ksn* values suggest the opposite (PEIFER; CREMON; ALVES, 2020; WHIPPLE et al., 2017).

The *ksn* was derived from channel slope and drainage area (slope-area or *S*–*A*) data obtained from FABDEM V1-2 using the gradient algorithm in TopoToolbox (SCHWANGHART & SCHERLER, 2014) for MATLAB R2023b, with θ_{ref}=0.45 (WOBUS et al., 2006; KIRBY; WHIPPLE, 2012). The average *ksn* values were then determined for each sampling catchment.

4. Results

4.1. Geomorphological characterization

Contiguous areas influenced by tectonic and lithological structures were grouped based on morphological similarities (SAADI et al., 2005; CORDEIRO; BASTOS; MAIA, 2018), leading to the classification of the massif's morphology into two main units: the High Surface and Low Surface. These units are further subdivided into smaller subunits, as illustrated in Figure 4.

The Pereiro Massif includes a Dissected Plateau, corresponding to the geomorphological unit occupying its highest sector. This region ranges in elevation from 600 m to the highest peaks (876 m) and is predominantly composed of monzogranites, granodiorites, and porphyritic granites. Elevated sectors of the massif also feature Planation Surfaces, marked by gabbroid suites at the summit of Pereiro, which exhibit a morphology distinct from surrounding structures.

The East Sideslope ranges in elevation from 400 to 600 m, with peaks reaching 700 m where the eastern escarpment rises. This escarpment features slopes exceeding 45°, forming the watershed divide between the Nazaré River and Santana River (Figure 4). Topographically, this unit exhibits slightly steeper slopes than the Dissected Plateau, with an average gradient of ~12°. Its undulating terrain follows a predominant NE-SW orientation (Figure 5), particularly evident near the Nazaré River sedimentary basin. Steep slopes are prominent on hillsides adjacent to the Sertaneja Surface, reflecting a stair-step topographic pattern at multiple elevations. Similar patterns occur in other Borborema Province massifs, such as the windward slopes of the Baturité Massif (BÉTARD; PEULVAST, 2011).

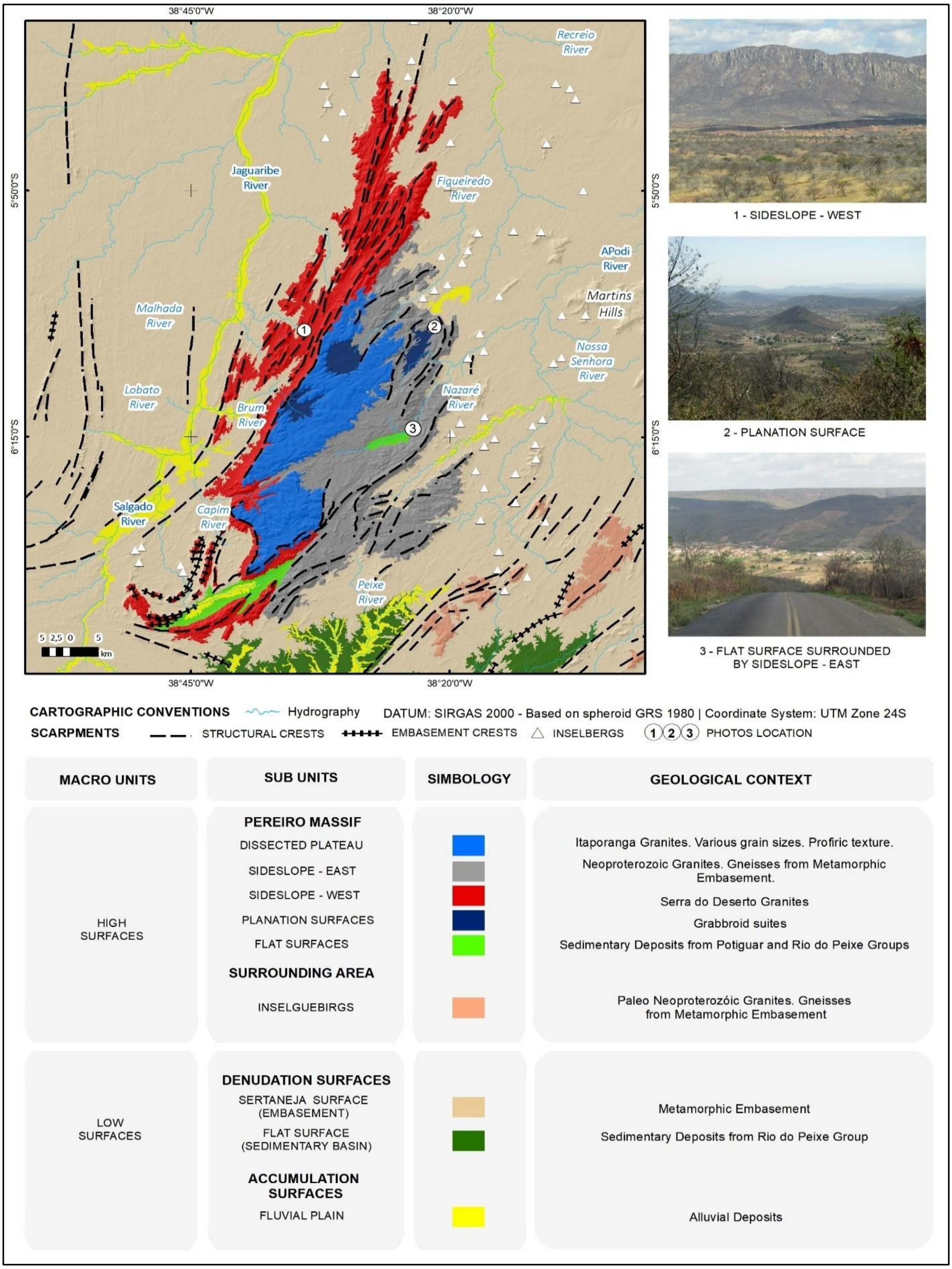

Figure 4. Geomorphological context of Pereiro Massif. DEM from FABEDEM (HAWKER et al. 2022); CPRM (2020); IBGE (2020).

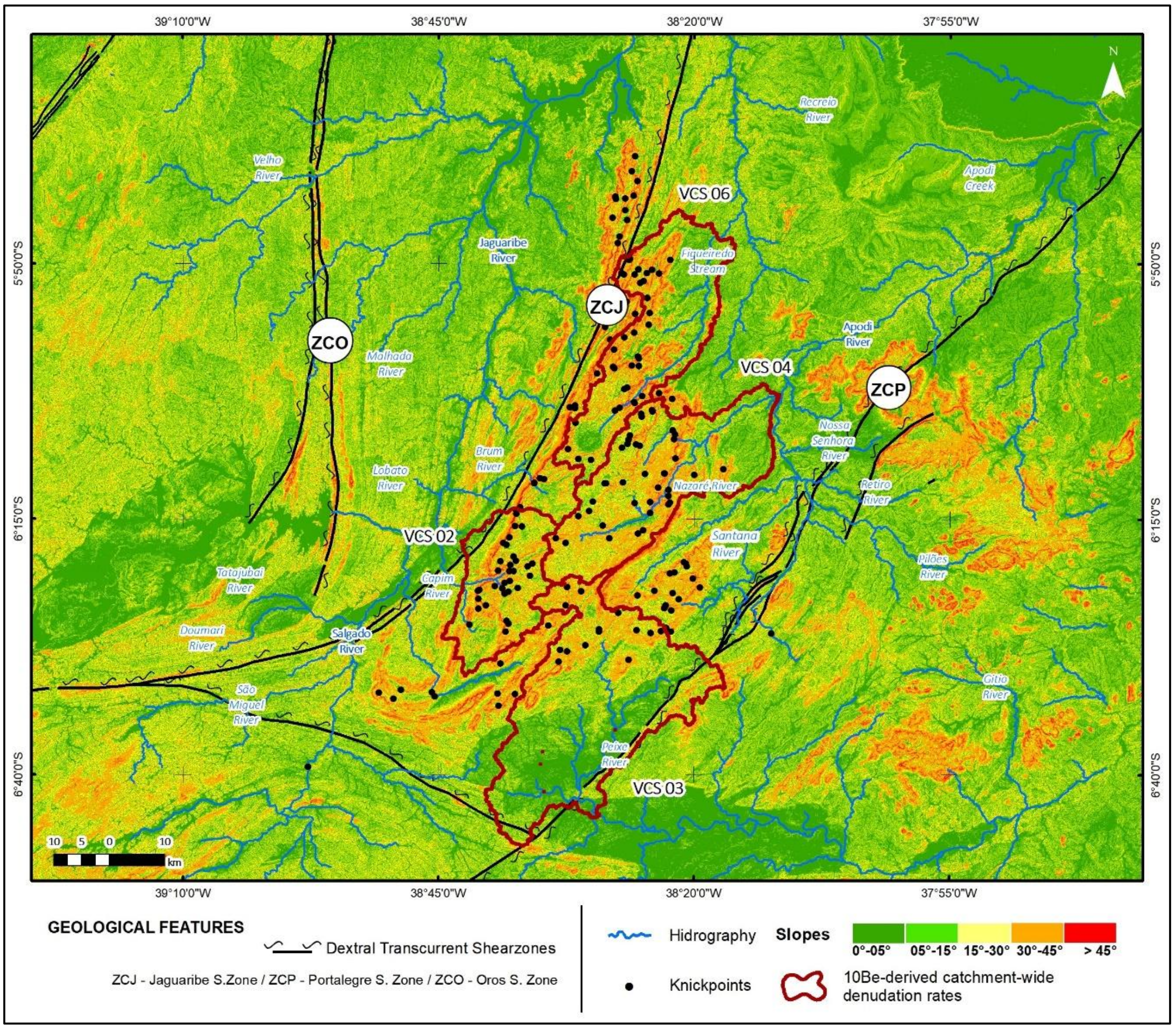

Figure 5. Slope context of Pereiro Massif (degrees) and knickpoint distribution. Plain surfaces highlighted in green; stepped terrains in yellow, orange, and red. Data sources: CPRM (2020); IBGE (2020); DEM from FABDEM (HAWKER et al., 2022).

The West Sideslope, a transitional zone between the Dissected Plateau and the central Sertaneja Surface of Ceará (CE), exhibits distinctive NE-SW-oriented elongated features influenced by the Jaguaribe Shear Zone. This unit is associated with dendritic drainage patterns flowing toward the Jaguaribe River.

In geological terms, this unit primarily consists of Statherian granites from the Serra do Deserto Suite, Ediacaran monzogranites from the Catingueira Suite, and granitoids from the Itaporanga Suite, which also form part of the Pereiro Massif. Additionally, granitoids from the Dona Inês Suite are present.

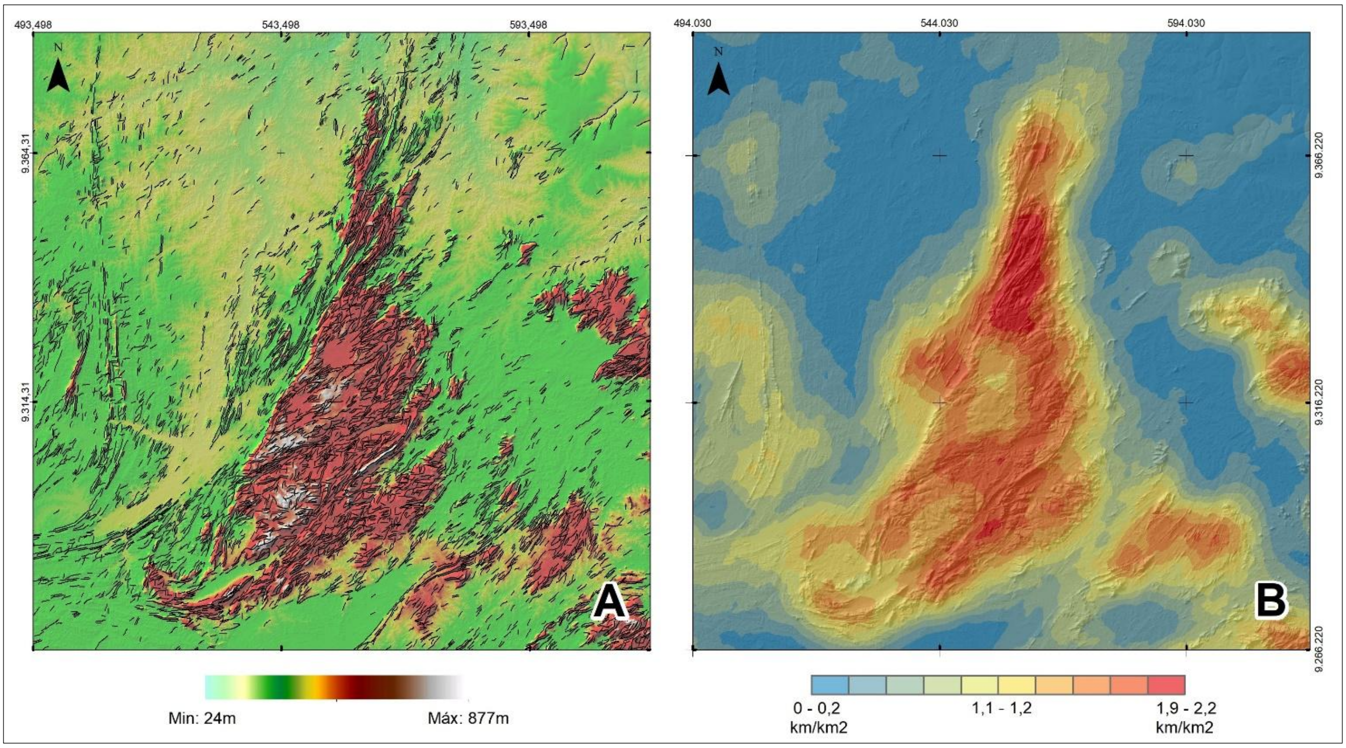

Figure 6. A. Lineaments identified in Pereiro Massif, contextualized with elevation ranges; B. Lineament density (km/km²). DEM from FABDEM (HAWKER et al., 2022).

The Cretaceous sedimentary basins of the Icozinho and Nazaré rivers are characterized by flat reliefs within the Pereiro Massif. Castro and Castelo Branco (1999) identify these basins as part of the Cariri-Potiguar trend (Matos, 1992), originating during the second syn-rift phase (Lower Barremian) of the South Atlantic system. Intense NW-SE crustal stretching during this phase generated NE-SW-oriented intracratonic sequences through distensional deformation (MATOS, 1992).

Basin geometry in this trend is defined by half-grabens separated by basement faults, transfer faults, and/or accommodation zones (CASTRO; CASTELO BRANCO, 1999). Sediments of the Nazaré River (Figure 4) reflect deposition from lateral retreat within the graben, driven by Cretaceous reactivations that formed horsts and semi-horsts via tectonism along the Orós-Jaguaribe fault system and Apodi transfer fault (PEULVAST et al., 2006). The basin's lithological substrate comprises sandstones, shales, and limestones of the Pendências Formation.

The Low Surfaces include the Denudation Surfaces (Sertaneja Surface and Flat Sedimentary Low Surfaces, situated atop the Cretaceous basins of the Iguatu and Peixe Rivers) and the Accumulation Surfaces (fluvial plains). The Sertaneja Surface surrounds the Pereiro Massif and represents Neogene denudation. It is characterized by elevations below 300 m and features residual landforms such as ridges, hills, and inselbergs, which originated from erosional processes acting on Neo- and Paleoproterozoic granitoids and quartzites (PEULVAST; CLAUDINO SALES, 2004).

Across its extent, the Sertaneja Surface exhibits landforms dissected by major river channels, leading to the formation of floodplains and terraces composed of alluvial deposits that include sandstones, shales, and silts. The main channels of the Salgado, Jaguaribe, and Apodi-Mossoró Rivers, the most significant rivers in the study area, are located within this unit. Additionally, tabular Cretaceous coverings from the Peixe, Iguatu, and Apodi River basins are present, formed through evolutionary processes involving graben and horst systems during Cenozoic reactivations (MAIA; BEZERRA, 2020).

4.2. Morphometric Analysis

The morphometric data for each analyzed river basin are presented in Table 1. The Compaction Ratio (*Kc*), Form Factor (*Kf*), and Circularity Index (*CI*) suggest that these units have a lower propensity for flood formation, indicating elongated and irregularly shaped basins. In such basins, rainfall tends to be distributed unevenly, leading to variations in infiltration rates and saturation times, which influence runoff formation and increase the concentration time of flow in the main channel (TUCCI, 2000).

The VCS02 basin, with *K*c and *Kf* values of 1.55 and 0.19, respectively, suggests a greater degree of circularity and, consequently, higher capacity for flow, entrenchment, and denudation. The VCS04 and VCS06 basins exhibited the highest number of knickpoints, which indicates geological conditions or processes modifying erosive rates, such as contrasting lithologies, base-level changes, or active structures (PEYERL et al., 2023).

In terms of drainage patterns, a predominance of dendritic patterns is observed (Figure 7). In the elevated zones of the Pereiro Massif, there is a notable correlation between drainage and negative lineaments, with a prevailing NE-SW and NW-SE orientation.

Table 1. Mophometric analysis results.

Parameters	Basin VCS02	Basin VCS03	Basin VCS04	Basin VCS06
Drainage area (km²)	118.6	1,353.7	719.9	596.9
Perimeter (km)	60.1	267.0	174.0	181.7
Compaction ratio (Kc)	1.55	2.03	1.82	2.08
Form ratio (Kf)	0.19	0.50	0.22	0.16
Circularity index (CI)	0.41	0.24	0.30	0.23
Drainage patterns	Dendritic	Dendritic	Dendritic	Dendritic
Orientation	West	South	Northeast	N- Northeast
Order of magnitude	3	5	5	5
Mean flow direction (degrees)	5.2°	2.1°	6.1°	8.9°
Mean slope (degrees)	10.06°	5.27°	8.13°	8.65°
Max slope (degrees)	62.54°	67.13°	50.39°	60.06°
Min river elevation (m)	179	251	183	95
Max river elevation (m)	568	347	439	544
Elevation range (m)	389	96	256	449
Total channel lenght (km)	118.5	982.25	693.32	600.11
Main river lenght (km)	21.02	52.01	57.15	60.46
Drainage density (k/km²)	1.00	0.98	0.96	0.95
Average *ksn*	35.19	9.53	19.98	21.05
Knickpoint quantity	26	14	40	36

In addition to the dendritic pattern, a significant occurrence of rectangular/trellis drainage is observed, primarily in areas with residual ridges on the drier western slope. Subparallel drainage patterns dominate the Eastern Sideslope region, particularly near the confluence of drainage systems into the Nazaré River. A radial drainage pattern is evident upstream of basin VCS06, coinciding with the Gabbroid Planation Surface.

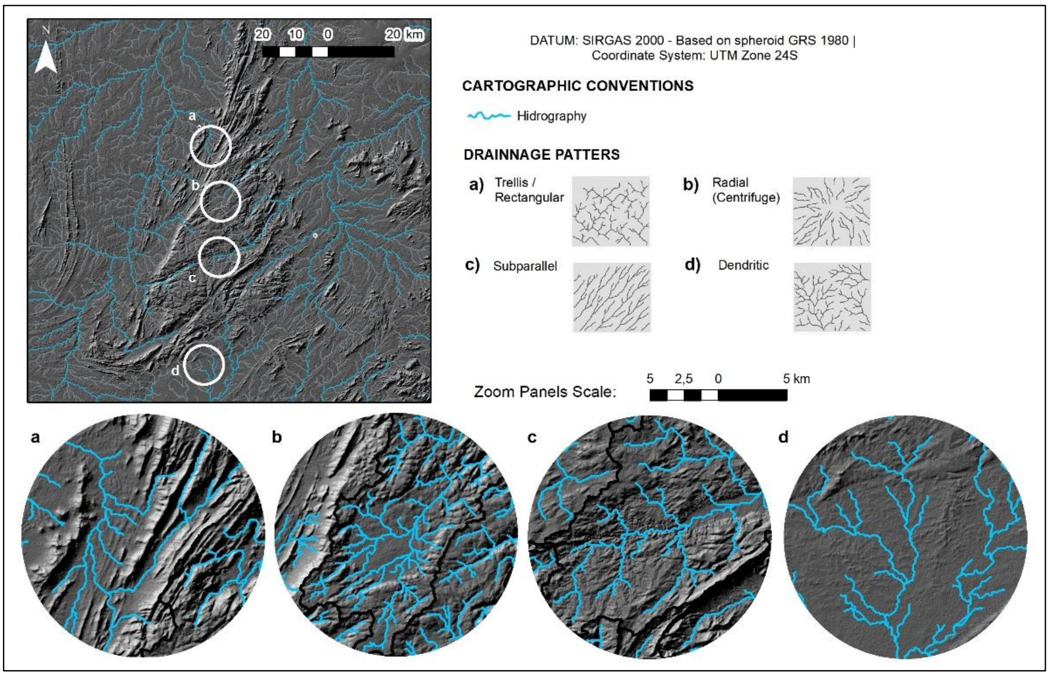

Figure 7. Drainage patterns identified in Pereiro Massif. Zoom panels: a. Trellis/Rectangular; b. Radial (centrifugal); c. Subparallel; d. Dendritic. Data sources: IBGE (2022); DEM from FABDEM (HAWKER et al., 2022).

Flow orientation (Figure 8) in basin VCS03 is notable for its lower average angle compared to other basins, reflecting its location on the Sertaneja Surface and gentle average slope (5.27°).

Basin VCS06 distinguishes itself with a significantly higher elevation range (average amplitude: 449 m), exceeding the second-highest basin (VCS02) by 60 m.

The *SL* method categorizes the analyzed rivers as being in "equilibrium", as indicated by *SLt*/*SL* values (Table 2; Figure 9), with all results below 2 (ETCHEBERE, 2006).

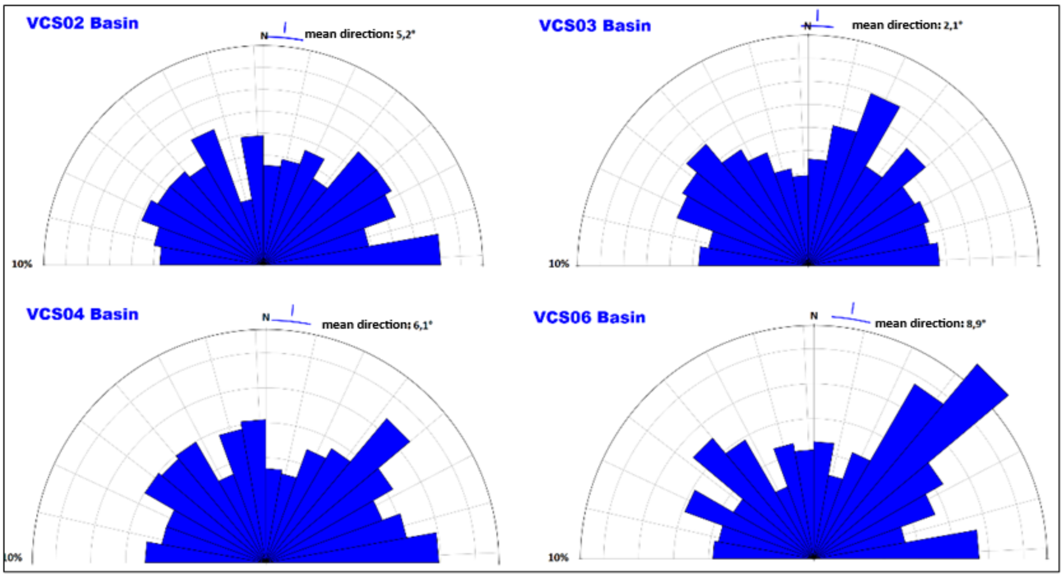

Figure 8. The preferential flow orientation exhibits little variation in the mean runoff direction across the analyzed basins.

Table 2. *SL* total values for the rivers analyzed.

Basin	River	H max. (m)	H min. (m)	ΔH (m)	L(km)	LognL	*SL* Total
VCS02	Capim River	568	179	389	21.02	3.23	120.45
VCS03	Peixe River	347	251	96	52.01	3.96	24.22
VCS04	Nazaré River	439	183	256	57.15	4.06	63.08
VCS06	Figueiredo	544	95	449	60.46	4.11	109.13

Min. and max. elevation in the basins (H min (m) / H max (m)) | Elevation range in (ΔH (m)) | Length of the river (L (km)) | Natural logarithm of L (LognL)

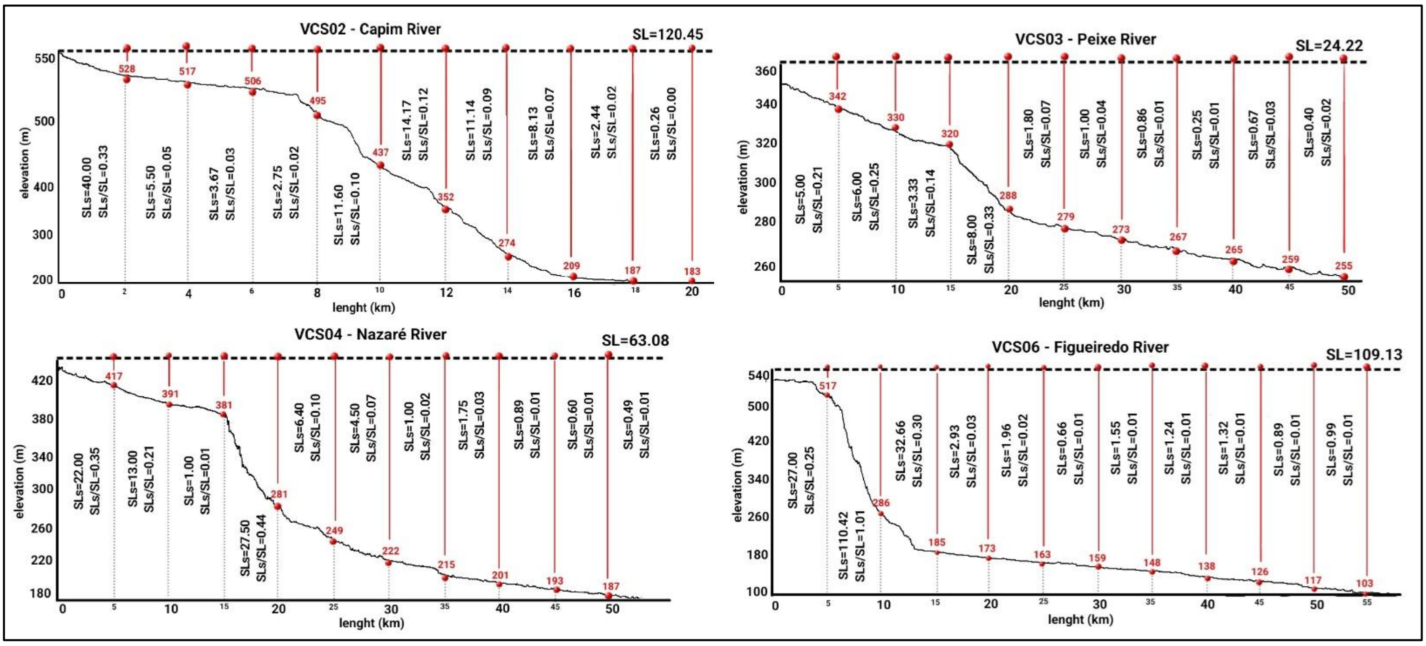

Figure 9. Longitudinal river profiles showing *SL* section results and their quotients relative to total SL.

4.3. Cosmogenic In-Situ Produced Data

Figure 10 presents the denudation rates of the analyzed basins. The basins include VCS06 (Figueiredo River) in the north, VCS04 (Nazaré River) in the east, VCS02 (Capim River) in the west, and VCS03 (Peixe River) in the south.

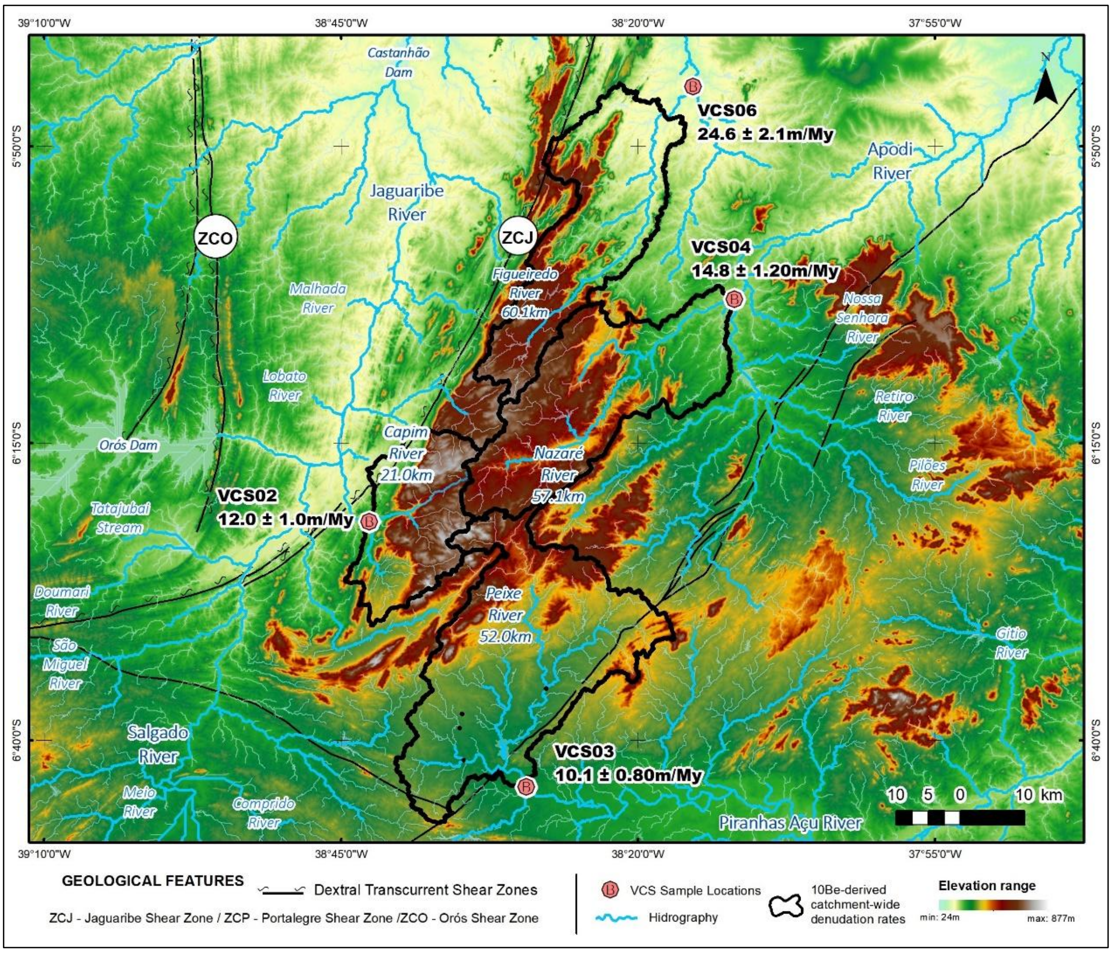

Figure 10. ^{10}Be samples location, river/erosion basins. Hydrological context with the length of each main river of the basins. IBGE (2022); CPRM (2020); DEM from FABEDEM (HAWKER et al., 2022).

Table 03 shows the values used in the denudation rate calculations. Among the sampled basins, VCS02 and VCS03 have the smallest and largest areas, respectively (118.58 and 1353.71km²), while basins VCS04 and VCS06 have the highest average slopes (150.70 and 164.96m/km).

Table 3. Basin areas, slopes, and total relief for the studied samples.

Sample ID	M.Slope	H. Min	H. Max	T. R.	Area	Av. H.	G.S.	S.F.S	M. Atm.P	Av. Pn.	Av. Ms	Av.
VCS02	17.82	200	870	670	118.58	454	0.9965	0.8473	959.86	3.39	0.014	0.044
VCS03	84.17	247	860	613	1353.71	355	0.9992	0.7823	971.33	3.14	0.014	0.043
VCS04	150.70	178	832	655	719.85	446	0.9983	0.8413	960.81	3.38	0.014	0.044
VCS06	164.96	107	792	685	596.92	357	0.9968	0.7890	971.09	3.16	0.014	0.043

Mean slope (m·km^{-1}) | H: Elevation Min and Max (m) | TR: Total Relief (m) | Area (km²) | Av. H: Average Elevation (m)
G.S: Geomorphic shielding | S.F.S: Scaling Factor Spallation | Mean Atm. P (mbar) |
Av. Pn: Average Production (at g^{-1} yr^{-1}) | Av. Ms: Average Muons (at g^{-1} yr^{-1}) | Av. Mf.: Average Muons Fast.: (at g^{-1} yr^{-1})

The values collected for the denudation rates of the basins (Table 04) indicate values of 10.1 ± 0.8 m·My^{-1} (VCS03), 12.0 ± 1.0 (VCS02), 14.8±1.2 m·My^{-1} (VCS04) and 24.6 ± 2.1 m·My^{-1} (VCS06).

Table 4. ^{10}Be data from Pereiro Massif samples.

Sample ID	Quartz Mass	M. ^{9}Be Add. *	B-C ^{10}Be/^{9}Be RU	^{10}Be C.	^{10}Be CU	Denudation rate (m·My^{-1})	Uncertainty D. rate (m·My^{-1})	Integration Time (yrs)	Uncertainty I. Time (yrs)
VCS02	20.36	0.8337	9.36E-15	227.1	7.694	12.0	1.0	54.049	4.352
VCS03	20.12	0.8327	1.03E-14	248.5	8.557	10.1	0.8	64.068	5.174
VCS04	20.18	0.8345	8,87E-12	186.6	7.357	14.8	1.2	43.953	3.649
VCS06	20.09	0.8341	6,15E-12	110.8	5.124	24.6	2.1	26.761	2.314
BLK	-	-	-	-	-	-	-	-	-

M. ^{9}Be Add.: Mass of ^{9}Be Added (g) | B-C ^{10}Be/^{9}Be R.: Background-Corrected ^{10}Be/^{9}Be Ratio

^{10}Be C.u.: ^{10}Be Concentration Uncertainty (atoms g-1) | *9Be was added through a carrier made at University of Vermont with a concentration of 304 μg ml-1.

*^{9}Be was added through a carrier made at University of Vermont with a concentration of 304 μg ml^{-1}.

**Isotopic analysis conducted at PRIME Lab.; Ratios normalized against standard 07KNSTD3110 with assumed ratio of 2850 x 10-15 (NISHIIZUMI et al., 2007).

***Propagated analytical uncertainties, 6% uncertainty on Sea-Level, High-latitude Production rate and 4% on surface material density (2.4±0.1)

4.4. Optically Stimulated Luminescence – OSL

Regarding the OSL samples, the location of the colluvial deposits and the values obtained are shown in Figure 11. The results of the samples (Table 5) indicate ages preferably related to the Holocene, ranging from 11.8Ky to 4.6Ky, with one sample dating from the Late Pleistocene period (14.06Ky).

Table 5. OSL – SAR sample ages for Pereiro Massif.

Equivalent Dose Information						
Sample	**ADR (uGy)**	**Dt (Gy)**	**ED (Gy)**	**OD (%)**	**Aliquots**	**Age (y)**
VCS LOE 02	8,150±200	2,7	37.9 ± 2.6	16 ± 4	10/10	4,645±335
VCS LOE 03	3,490±130	3,6	41.3 ± 2.2	9 ± 2	10/10	11,835±760
VCS LOE 04	3,370±120	2,7	47.4 ± 2.9	13 ± 3	10/10	14,060±975
VCSLOE 05	4,680±150	3,6	55.2 ± 3.7	15 ± 4	10/10	11,805±875
VCSLOE 06	4,700±140	2,7	55.4± 3.3	13 ± 3	10/10	11,785±790

ADR – Annual dose rate | Dt - Dose test | ED - Equivalent dose | OD - Overdispersion

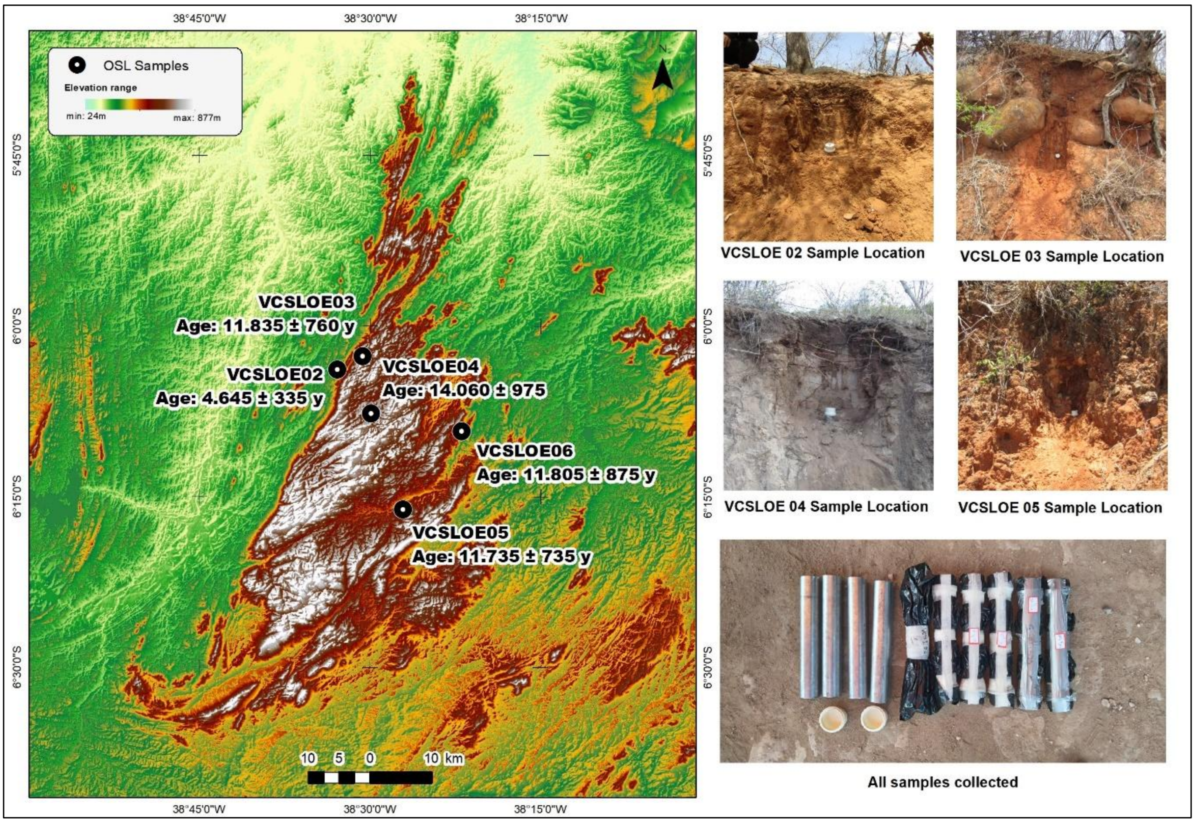

Figure 11. OSL sample locations and measured ages. DEM from FABDEM (HAWKER et al., 2022).

The samples exhibited average values of 3.342ppm for Uranium (U), 11.18ppm for Thorium (Th), and 3.26% for Potassium (K). These values are characteristic typically indicate compositions rich in silica, such as feldspars and apatites (TUDELA et al., 2011).

Table 6. OSL – SAR sample ages for Pereiro Massif.

Field Information					Dose Rate Information					
Sample	H (m)	Coordinates E	Coordinates N	Depth (m)	U (ppm)	Th (ppm)	K (ppm)	WC (%)	DR (mGy/yr)	CDR (uGy/yr)
VCS LOE 02	224	549915	9329685	1,5±0,15	7.4±0.4	28.7±0.9	4.3±0.1	0.9±0.1	8.1±0.2	160±20
VCS LOE 03	503	554280	9331828	1,5±0,15	2.7±0.2	8.3±0.3	2.2±0.1	3.1±0.3	3.5±0.1	170±20
VCS LOE 04	560	555280	9322542	1,5±0,15	1.4±0.1	3.2±0.2	2.6±0.1	0.0±0.0	3.3±0.1	180±20
VCSLOE 05	422	560472	9307063	1,5±0,15	1.9±0.1	4.6±0.2	3.0±0.1	0.9±0.1	4.7±0.1	170±20
VCSLOE 06	415	570235	9319605	1,5±0,15	3.3±0.2	11.1±0.4	3.0±0.1	0.0±0.0	4.7±0.1	170±20

H - Elevation (m) ǀ U - Uranium ǀ Th - Thorium ǀ K - Potassiumǀ WC - Water content ǀ DR – Dose rate ǀ CDR - Cosmic dose rate ǀ

Figure 12 shows the results of the dose recovery tests in a diagram with their corresponding Galbreith radial plots, highlighting the consistency of the data obtained for the OSL ages, as all the aliquots measured are between 0.9 and 1.1, i.e. less than 10% variation.

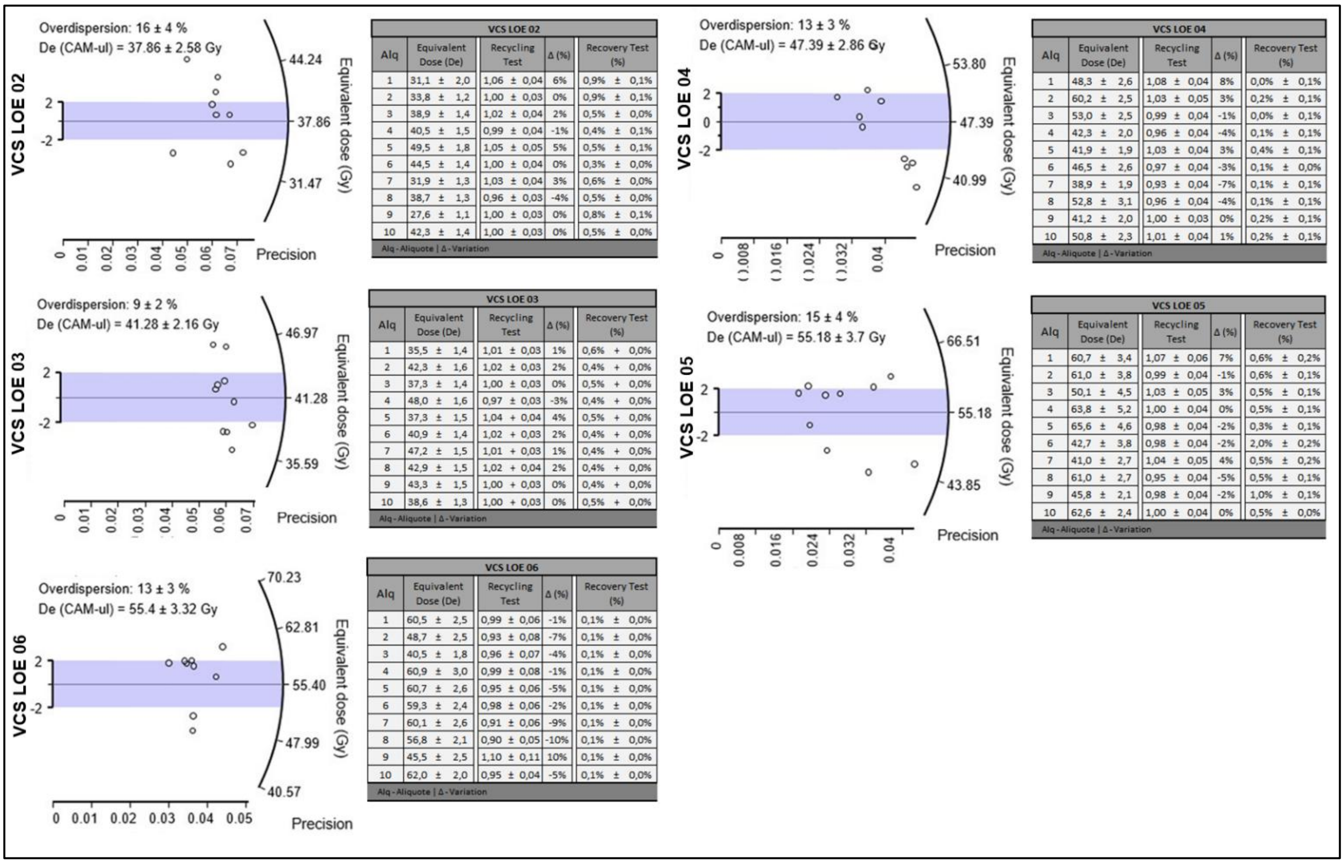

VCS LOE 02				
Alq	Equivalent Dose (De)	Recycling Test	Δ (%)	Recovery Test (%)
1	31,1 ± 2,0	1,06 ± 0,04	6%	0,9% ± 0,1%
2	33,8 ± 1,2	1,00 ± 0,03	0%	0,9% ± 0,1%
3	38,9 ± 1,4	1,02 ± 0,04	2%	0,5% ± 0,0%
4	40,5 ± 1,5	0,99 ± 0,04	-1%	0,4% ± 0,1%
5	49,5 ± 1,8	1,05 ± 0,05	5%	0,5% ± 0,1%
6	44,5 ± 1,4	1,00 ± 0,04	0%	0,3% ± 0,0%
7	31,9 ± 1,3	1,03 ± 0,04	3%	0,6% ± 0,0%
8	38,7 ± 1,3	0,96 ± 0,03	-4%	0,5% ± 0,0%
9	27,6 ± 1,1	1,00 ± 0,03	0%	0,8% ± 0,1%
10	42,3 ± 1,4	1,00 ± 0,03	0%	0,5% ± 0,0%
Alq - Aliquote | Δ - Variation				

VCS LOE 04				
Alq	Equivalent Dose (De)	Recycling Test	Δ (%)	Recovery Test (%)
1	48,3 ± 2,6	1,08 ± 0,04	8%	0,0% ± 0,1%
2	60,2 ± 2,5	1,03 ± 0,05	3%	0,2% ± 0,1%
3	53,0 ± 2,5	0,99 ± 0,04	-1%	0,0% ± 0,1%
4	42,3 ± 2,0	0,96 ± 0,04	-4%	0,1% ± 0,1%
5	41,9 ± 1,9	1,03 ± 0,04	3%	0,4% ± 0,1%
6	46,5 ± 2,6	0,97 ± 0,04	-3%	0,1% ± 0,0%
7	38,9 ± 1,9	0,93 ± 0,04	-7%	0,1% ± 0,1%
8	52,8 ± 3,1	0,96 ± 0,04	-4%	0,1% ± 0,1%
9	41,2 ± 2,0	1,00 ± 0,03	0%	0,2% ± 0,1%
10	50,8 ± 2,3	1,01 ± 0,04	1%	0,2% ± 0,1%
Alq - Aliquote | Δ - Variation				

VCS LOE 03				
Alq	Equivalent Dose (De)	Recycling Test	Δ (%)	Recovery Test (%)
1	35,5 ± 1,4	1,01 ± 0,03	1%	0,6% + 0,0%
2	42,3 ± 1,6	1,02 ± 0,03	2%	0,4% + 0,0%
3	37,3 ± 1,4	1,00 ± 0,03	0%	0,5% + 0,0%
4	48,0 ± 1,6	0,97 ± 0,03	-3%	0,4% + 0,0%
5	37,3 ± 1,5	1,04 + 0,04	4%	0,5% + 0,0%
6	40,9 ± 1,4	1,02 + 0,03	2%	0,4% + 0,0%
7	47,2 ± 1,5	1,01 + 0,03	1%	0,4% + 0,0%
8	42,9 ± 1,5	1,02 + 0,04	2%	0,4% + 0,0%
9	43,3 ± 1,5	1,00 + 0,03	0%	0,4% + 0,0%
10	38,6 ± 1,3	1,00 + 0,03	0%	0,5% + 0,0%
Alq - Aliquote | Δ - Variation				

VCS LOE 05				
Alq	Equivalent Dose (De)	Recycling Test	Δ (%)	Recovery Test (%)
1	60,7 ± 3,4	1,07 ± 0,06	7%	0,6% ± 0,2%
2	61,0 ± 3,8	0,99 ± 0,04	-1%	0,6% ± 0,1%
3	50,1 ± 4,5	1,03 ± 0,05	3%	0,5% ± 0,1%
4	63,8 ± 5,2	1,00 ± 0,04	0%	0,5% ± 0,1%
5	65,6 ± 4,6	0,98 ± 0,04	-2%	0,3% ± 0,1%
6	42,7 ± 3,8	0,98 ± 0,04	-2%	2,0% ± 0,2%
7	41,0 ± 2,7	1,04 ± 0,05	4%	0,5% ± 0,2%
8	61,0 ± 2,7	0,95 ± 0,04	-5%	0,5% ± 0,1%
9	45,8 ± 2,1	0,98 ± 0,04	-2%	1,0% ± 0,1%
10	62,6 ± 2,4	1,00 ± 0,04	0%	0,5% ± 0,0%
Alq - Aliquote | Δ - Variation				

VCS LOE 06				
Alq	Equivalent Dose (De)	Recycling Test	Δ (%)	Recovery Test (%)
1	60,5 ± 2,5	0,99 ± 0,06	-1%	0,1% ± 0,0%
2	48,7 ± 2,5	0,93 ± 0,08	-7%	0,1% ± 0,0%
3	40,5 ± 1,8	0,96 ± 0,07	-4%	0,1% ± 0,0%
4	60,9 ± 3,0	0,99 ± 0,08	-1%	0,1% ± 0,0%
5	60,7 ± 2,6	0,95 ± 0,06	-5%	0,1% ± 0,0%
6	59,3 ± 2,4	0,98 ± 0,06	-2%	0,1% ± 0,0%
7	60,1 ± 2,6	0,91 ± 0,06	-9%	0,1% ± 0,0%
8	56,8 ± 2,1	0,90 ± 0,05	-10%	0,1% ± 0,0%
9	45,5 ± 2,5	1,10 ± 0,11	10%	0,1% ± 0,0%
10	62,0 ± 2,0	0,95 ± 0,04	-5%	0,1% ± 0,0%
Alq - Aliquote | Δ - Variation				

Figure 12. Recycling and recovery dose test results plotted on Galbraith's Radial Plot for all OSL samples.

5. Discussion

The lithological configuration of the eastern Pereiro Massif—comprising porphyritic granites, diorites, gabbros, gneisses, and quartz-biotite assemblages—suggests that denudation processes have generated a stepped geomorphological pattern due to differential resistance among lithologies. Prominent features, such as the eastern scarps, persist as remnants of more resistant lithotypes. These scarps, as proposed by Peulvast et al. (2006), likely represent residual structures of Ediacaran horst systems formed during syn-orogenic uplift.

The Serra do Deserto Granites associated with the dissected plateau and the eastern escarpment suggest that this magmatic suite acts as a barrier against regressive erosion, preserving the elevated features observed in the Pereiro Massif. These findings align with conclusions by Cordeiro (2017) regarding the evolution of the Quincuncá Massif, another granitic body in the northern sector of the Borborema Province.

The planation surfaces within the Gabbroid Suites (Figure 4)—characterized by mafic composition, phaneritic texture, medium-to-coarse grain size, and low quartz/silica content—suggest their morphology results from greater vertical lowering relative to the adjacent, more resistant Ediacaran granites. This interpretation matches observations by Cordeiro (2017) in the Quincuncá Massif (CE), where a lowered tabular gabbroid surface occupies the central portion of the massif, surrounded by higher granitic terrains, and in the Pedra Aguda Inselberg (CE), a granitic dome encircled by erosive gabbroid surfaces (BASTOS; CORDEIRO, 2021). These features indicate elevation reduction due to mechanical erosion processes, attributed to the lower resistance of gabbros and diorites composing these suites (CORDEIRO; BASTOS; MAIA, 2018). Consequently, this resulted in flat relief within the dissected plateau's broader topography.

Another notable characteristic of this unit is its correlation with springs in microdrainage basins. This correlation implies that erosional processes acting on the less resistant gabbroid suites caused pronounced vertical lowering and marginal retreat compared to surrounding lithotypes, forming planar surfaces. Bastos and Cordeiro (2021) emphasize a direct link between mineral composition and the morphological evolution of granitic exposures at regional scales. They further note that crystal size directly influences erosion rates, with porphyritic granites being less resistant to disintegration than haplogranites.

The denudation values for the basins indicate more intense denudation in the northern and eastern parts of the massif. In basins VCS04 and VCS06, erosion rates were 14.8±1.2 m·My^{-1} and 24.6±2.1 m·My^{-1}, respectively, while basins VCS02 and VCS03 exhibited the lowest sampled rates (12.0±1.0 m·My^{-1} and 10.1±0.8 m·My^{-1}). These results suggest greater lithological resistance to erosion in the western and southern regions of the Pereiro Massif. The denudation rates derived from in situ ^{10}Be are integrated over a Late Pleistocene timescale, spanning 27±2 to 64±5 kyr.

The lowest denudation rate in the VCS03 basin (10.1±0.8 m·My^{-1}) may reflect its topographic context, characterized by lowered sectors that promote erosive stabilization along the longitudinal profile (Figure 12). In contrast, basins VCS02, VCS04, and VCS06 are situated on steeper slopes of the massif, where gravitational instability drives higher denudation. The highest rate in VCS06 (24.6±2.1 m·My^{-1}) likely results from lithological diversity, structural lineament density (Figure 6), and enhanced fluvial dissection.

When comparing denudation rates to morphometric parameters, basin VCS02 shows the highest average slope (10.06°) and normalized steepness index (*ksn*=35.19), yet its denudation rate (12.0±1.0 m·My^{-1}) is the second lowest. This discrepancy may reflect the greater resistance of Itaporanga Suite granitoids.

Basin VCS03, with the lowest denudation rate (10.1±0.8 m·My^{-1}), aligns with its gentle slopes (5.27°), low *ksn* (9.53), and minimal knickpoints (14), consistent with stabilized morphodynamics on lowered surfaces.

Basin VCS04, draining the eastern massif, has the second-highest denudation rate (14.8±1.2 m·My^{-1}), the most knickpoints (40), moderate slope (8.13°), and *ksn* (19.98). These features reflect lithological variability and NE-trending structural controls.

Basin VCS06, in the northern massif, records the highest denudation rate (24.6±2.1 m·My^{-1}), moderate slope (8.65°), *ksn* (21.05), and abundant knickpoints (36), likely due to NE structural deformation and lithological heterogeneity.

The denudation rates determined by in situ produced ^{10}Be for the Pereiro basins (ranging from 10.1 ± 0.80 to 24.6 ± 2.10 m·My^{-1}) indicate slow to moderate rates of denudation. These values are consistent with those observed in other passive margin landscapes. Linari et al. (2017) reported erosion rates ranging from 5.4 to 49 m·My^{-1} in the central portion of the Appalachian Blue Ridge chain. Similarly, the Great Smoky Mountains exhibit rates between 5 and 48 m·My^{-1} (MATMON et al., 2003). In Namibia, erosion rates range from 1.51 to 14.6 m·My^{-1} (BIERMAN; CAFFEE, 2001; BIERMAN et al., 2007), while the Potomac and Susquehanna regions show rates between 2.8 and 66 m·My^{-1} (DUXBURY et al., 2015). In Australia, erosion rates range from 8.3 to 51.9 m·My^{-1} (HEIMSATH et al., 2006), whereas Madagascar displays rates from 5.8 to 22.3 m·My^{-1} (COX et al., 2009).

In comparison, studies in active margin zones typically report much higher erosion rates than those observed in passive margins. For example, Palumbo et al. (2011) documented rates of 833 ± 68 m·My^{-1} in the Qilian Shan region (northeastern Tibet), while Portenga et al. (2015) recorded rates as high as 956 ± 160 m·My^{-1} in western Bhutan (Himalayas). Similarly, Rossi et al. (2017) reported 353 ± 119 m·My^{-1} in Sierra San Pedro Mártir, Baja California.

Climatically analogous regions, such as the semi-arid Flinders Ranges (Australia), yield comparable denudation rates. In the Yudnamutana Gorge Basin, in situ ^{10}Be concentrations in modern alluvial sediments around granitic inselbergs indicate an average erosion rate of 22.79 ± 2.78 m·My^{-1} (QUIGLEY et al., 2007).

In the national context, the erosion rate values identified for the Pereiro Massif are consistent with rates recorded in various regions across Brazil. These rates align with those observed in the Serra do Mar escarpments (8.1 to 47.7 m·My^{-1}, SALGADO et al., 2014), the basins of Serra dos Órgãos, Mantiqueira, and Serra Geral (13 to 90 m·My^{-1}, GONZALEZ et al., 2016), the Cristiano Otoni and São Geraldo escarpments (5.21 to 23.7 m·My^{-1}, CHEREM et al., 2012), the Rio Grande and Paraíba do Sul basins (7.55 to 26.5 m·My^{-1}, REZENDE et al., 2013), the basins of the Itajaí-Açu, Iguaçu, and Uruguai Rivers (3.8 to 58.8 m·My^{-1}, SORDI et al., 2018), and the basins of the Paraná and Ivaí Rivers (6.4 to 10.9 m·My^{-1}, COUTO et al., 2018). It is important to note that these regions exhibit distinct morphoclimatic characteristics when compared to the Brazilian semiarid region.

In the regional context, the erosion rates observed in Pereiro align with those reported by Peulvast, Bétard, and Lageat (2009) regarding the dissection of the Cariri–Potiguar footwall uplands and the expansion of the erosional Sertaneja Surface and coastal plains, where erosion rates reach up to <10 m·My^{-1}, based on morphostratigraphic analyses. Similarly, Jelinek et al. (2014, 2020) documented erosion rates of 10–30 m·My^{-1} in various regions, including the southern Borborema Plateau, Conquista and Jequitinhonha Plateaus, Sertaneja

Surface, Recôncavo-Tucano-Jatobá Rift, and Diamantina Plateau, derived from apatite fission-track thermochronology and reflecting long-term denudation rates.

The correlation between erosion rates and the geomorphic data of the basins indicates a consistent pattern. The data suggest that denudation is more intense in basins with a lower tendency to flooding, such as VCS02, VCS04, and VCS06, which have elongated and irregular shapes. These basin characteristics imply longer channel saturation times before overflow occurs, as described by Tucci (2000). In contrast, VCS03, which exhibits a higher degree of roundness, lower average slope, lower *ksn* values, and fewer knickpoints, experiences less intense erosion.

Considering that denudation rates were higher during the Cretaceous rifting period (PEULVAST; CLAUDINO SALES, 2004) and that the post-rift phase has shown extremely low values at a regional scale (PEULVAST; BÉTARD, 2013), indicating slow denudation, Peulvast and Bétard (2021) identified factors that may explain the slow evolution of the Brazilian Northeast relief and its influence on escarpment formation. These factors include: (i) Low magnitude of crustal uplift; (ii) Low amplitude and long wavelength of crustal deformation in initially flat terrain, favoring morphological resistance (BRUSDEN, 1993); and (iii) High lithological resistance of basement rocks (granites and orthogneisses) and sedimentary basins (sandstones and limestones) to weathering processes, leading to the preservation of residual reliefs at high elevations.

The Sideslope East exhibited the highest erosion rates in the eastern and northern basins (VCS04 and VCS06, with 14.8 ± 1.2 m·My^{-1} and 24.6 ± 2.10 m·My^{-1}, respectively). These areas have average slopes of 8.13° and 8.65°, with some locations exceeding 60°. The presence of various lithological compositions, including orthogneisses, paragneisses, granodiorites, and schists, covering over 42% of the area, makes these slopes less resistant compared to the granites of the Itaporanga Suite (BASTOS; CORDEIRO, 2021). This lower resistance likely explains the higher erosion rates observed in this area, along with the observed NE-SW lateral retreat, which indicates a faster evolution of the terrain in this orientation, in correlation with the windward section of the massif.

Although the VCS02 basin has the highest average slope (10.06°) and overall *SL* index, it exhibits the second-lowest erosion rate (12.0 ± 1.0 m·My^{-1}). This discrepancy may stem from its small basin area (118.5 km²) and short main river length (21.02 km), resulting in a drainage network with lower capillarity and erosive capacity relative to the rocky substrate. This substrate, composed of 74% Ediacaran granites from the Itaporanga Suite, dominates the dry slope area of the basin.

In contrast, the VCS03 basin has the lowest erosion rate (10.8 ± 0.8 m·My^{-1}), gentler slopes (5.27°), a larger area (1,354 km²), and a longer main river (52.01 km). Its lithology includes gneisses, schists, sandstones, and limestones from the Antenor Navarro and Santana Formations, significantly influenced by the Portalegre Shear Zone.

The VCS04 and VCS06 basins share similar morphometric parameters, with areas of 719 km² and 596 km², average slopes of 8.13° and 8.65°, and river lengths of 57.15 km and 60.46 km, respectively. The key difference lies in their elevation (256 m vs. 449 m), which, combined with the high total *SL* index of VCS06 (109.13), may explain its higher denudation rate. The elevated *SL* index indicates greater river power, likely contributing to enhanced erosional efficiency.

In absolute terms, while the Capim River is the shortest, the Peixe, Figueiredo, and Nazaré Rivers are 2.5, 2.7, and 2.9 times longer, respectively, with basins 11.5, 6.0, and 5.0 times larger. However, these dimensions alone do not directly correlate with denudation rates. For example, the lowest rates (VCS02: 12.0±1.0 m·My^{-1}; VCS03: 10.8±0.8 m·My^{-1}) correspond to the smallest (Capim River) and largest (Peixe River) basins, yet their rates are statistically similar within uncertainty limits. The denudation rates of VCS02 and VCS03 are only 1.2 and 2.0 times lower than those of VCS04 and VCS06, respectively. Thus, these values must be contextualized with geological, climatic, and morphometric factors to be fully understood.

The erosion rates recorded for the Pereiro Massif align with the proposed evolutionary model for Jaguaribean terrains (CAVALCANTE, 1999), particularly the Ediacaran granite suites found in Central Ceará and Rio Grande do Norte. These rates highlight the role of Cretaceous and Cenozoic reactivations as drivers of morphogenetic processes in the massifs, shaped by paleoclimatic fluctuations during alternating interstadial and stadial stages.

Since the Neogene, regional semi-aridity has been the dominant climate (MORAIS NETO et al., 2005; HARRIS; MIX, 2002), punctuated by wetter intervals (BEHLING et al., 2000; WANG et al., 2004). Consequently, both current and past climatic conditions are critical to understanding the evolution of the morphological features observed in the Pereiro Massif.

The semiarid context of the study area is characterized by significant annual rainfall irregularities, which are influenced by regional orographic factors. In this setting, the presence of eastern windward slopes is a common feature in the massifs of the Borborema Province, where wetter conditions prevail. This pattern is also observed in the Pereiro Massif, where the eastern sector receives an average annual rainfall of 1,097 mm (CEARÁ, 2017). This rainfall distribution influences soil formation, vegetation cover, and denudation rates, which tend to be higher in drier (leeward) sectors.

The OSL age results from the Pereiro samples suggest important colluvial deposition periods associated with climatic variations between the Last Glacial Maximum (LGM) and the Younger Dryas, covering Marine Isotope Stages 1 and 2 (MIS 1 and 2). This period is marked by phases of increased humidity in the Brazilian Northeast (ZHANG et al., 2017; VENANCIO et al., 2020; AULLER; SMART, 2001).

It can be inferred that the transition to colder and drier paleoclimatic conditions intensified erosion processes, leading to colluvium deposition on the massif's slopes. These hypotheses align with findings from studies on alluvial and aeolian deposits in the post-Barreiras portion of the northeastern coast (TUDELA et al., 2011; ROCCA et al., 2012; XIMENES NETO et al., 2024) and fluvial terraces in the Parnaíba Basin (SAWAKUCHI, 2016). Furthermore, it is likely that these deposits are linked to the transition from a wetter phase recorded around 15,000 years ago—associated with Heinrich Stage 1 (HS1) (WANG et al., 2004)—to a subsequent drier phase, likely corresponding to the Younger Dryas, which led to the removal of weathering mantles formed during the preceding humid period.

Considering the potential correlations between sample ages and past global climate changes, the colluvium in the Pereiro Massif appears to be consistent with the findings of Sallum and Suguio (2010). Their study suggests that at the onset of arid cycles, such as the one inferred for the Last Glacial Maximum (LGM) (PETIT et al., 1999), soil layers previously stabilized by leafy vegetation were remobilized, making them more vulnerable to denudation. This process led to the rapid and intense reworking of sediments deposited on steeper slopes during the transition to the interglacial period, coinciding with intensified precipitation events in northeastern Brazil associated with the HS1 and Younger Dryas events (WELLS et al., 1987; BULL; VAN DONK, 1970). Furthermore, the mid-Holocene aridification in Northeast Brazil (UTIDA et al., 2020) likely played a significant role in this colluvial deposition process.

The analysis of the *SL* index indicates that neotectonic structural components do not influence the river courses, with erosion processes being the predominant factor in shaping their morphologies. In the Pereiro Massif, fault zones, lithological diversity, and other lineaments act as primary structural controls on river morphology, in line with the regional geological framework of the Borborema Province (MAIA; BEZERRA, 2020; CORDEIRO; BASTOS; MAIA, 2018). Drainage systems controlled by structurally unaffected lineaments, not influenced by neotectonism, exhibit equilibrium in relative drainage energy (SL), characterized by stabilized concave profiles (Figure 9) and an absence of abrupt topographic breaks in river thalwegs. This hydro-geomorphological behavior is also observed in other rivers in northwestern Ceará (BELARMINO; BASTOS, 2021).

Regarding the morphostructural aspects in the interpretation of the Pereiro Massif, Gurgel (2012) posits that neotectonic events played a role in the formation of denudation basins surrounding the massif, such as the Merejo Basin, and in the lateritic cover, which he considers strong evidence of local tectonic uplift along shear zones that may have been reactivated during the Cenozoic. According to this interpretation, movement along these shear zones is the primary morphostructural factor shaping the massif.

However, Peulvast and Bétard (2013) present a different perspective, arguing that the lateritic cover does not constitute definitive evidence of local uplift, as such features can develop in various altitudinal and topographic contexts (ROSSETTI, 2004). This reinforces the understanding that the morphological evolution of the massif does not exhibit significant signs of neotectonic reactivations. Instead, it is plausible to interpret the massif as a product of structural and lithological constraints, with climatic events, such as the LGM, HS1, and Younger Dryas, acting as major erosive milestones.

Peulvast and Bétard (2013) also note that displacement rates recorded on active faults in the northeastern coastal zone, ranging from 0.0075 to 0.01 mm·year^{-1}, have accumulated to approximately 180 m of vertical displacement in the Cretaceous basins of Paraíba (NOGUEIRA; BEZERRA; FUCK, 2010). These values suggest very subtle and localized neotectonic contributions, which, when considering the formation of ridges and massifs farther from seismic epicenters, appear insufficient to account for significant morphostructural changes. Furthermore, the concept of strong neotectonism does not align with the presence of Cretaceous-aged paleopiedmont, which has been exhumed and remains undeformed in the northern portion of the massif (PEULVAST; CLAUDINO SALES, 2004).

The *SL* data from the analyzed river channels further support this interpretation of inherited morphologies, as the absence of first- or second-order anomalies suggests a lack of local neotectonic uplifts. The drainage patterns appear to be entrenched or parallel to the lineaments, reinforcing the notion that their development is structurally controlled rather than neotectonically influenced.

Additionally, Peulvast et al. (2006) support the Cretaceous evolution theory, proposing that the eastern and western sections of the Pereiro Massif can be characterized as part of a horst or semi-horst system, formed by the tectonic activity of the Orós-Jaguaribe fault system and the Apodi transfer fault to the northeast. According to this model, the current topographic edges correspond to the external contacts of granitic intrusions, which are found up to 40 km from the main faults.

6. Conclusion

In summary, the exposure of plutonic bodies in the Borborema Province resulted from the denudation and reworking of previously orogenic terrains. The denudation processes analyzed through cosmogenic isotopes and morphometric analyses corroborate earlier interpretations (PEULVAST; CLAUDINO-SALES, 2004; PEULVAST et al., 2006), which suggest tectonic stability throughout the Cenozoic.

Therefore, it is reasonable to assume that, due to differential erosion and the structural trends imposed by the Jaguaribe and Portalegre shear zones, the contrast between the marginal metamorphic features and the plutonic granitoid core of the Pereiro Massif facilitated its exhumation. This exhumation, along with the orientation of specific punctual and elongated residual ridges, as well as deeply dissected valleys shaped by erosive agents (CORRÊA et al., 2010)—particularly the outflows from the northeastern and eastern portions of the massif—demonstrates the clear structural control over denudation processes that have shaped the relief.

The main uplifts related to the Pereiro Massif are linked to the phases of Pangea's breakup during the Cretaceous, which generated regional uplifts in the northern sectors of the Borborema Province. Consequently, the Pereiro Massif can be considered a geomorphological compartment inherited from these uplifts, with its Cenozoic denudational evolution being primarily controlled by structural lineaments and lithological constraints.

Author's contributions: Conception: BRITO, E. R., BASTOS, F. H., CLAUDINO SALES, V. C.; Methodology: BRITO, E. R., BASTOS, F. H., SIAME, L.; Software and Geoprocessing: BRITO, E. R.; Validation: BASTOS, F. H., CLAUDINO SALES, V. C., SIAME, L. L., CORDEIRO, A. M. N.; Fieldwork: BRITO, E. R., CLAUDINO SALES, V. C., BASTOS, F. H., CORDEIRO, A. M. N.; Research: BRITO, E. R., BASTOS, F. H., CLAUDINO SALES, V. C. CORDEIRO, A. M. N.; Article Writing: BRITO, E. R., BASTOS, F. H., SIAME, L. L.; Review: BASTOS, F. H., CLAUDINO SALES, V. C., SIAME, L. L., CORDEIRO, A. M. N.; Supervision: BASTOS, F. H. All authors read and agreed with the published version of the manuscript.

Funding: This research was funded by the National Council for Scientific and Technological Development (CNPq – Projects No 405982-2018-6, 403944/2023-6 and 310887/2021-6) and the Ceará Foundation for Scientific and Technological Development Support (FUNCAP – Project No UNI-0210-00042.01.00/23).

Acknowledgments: The authors thank the Graduate Program in Geography of the State University of Ceará (ProPGeo/UECE) for logistical support, the National Council for Scientific and Technological Development (CNPq), the Ceará Foundation for Scientific and Technological Development Support (FUNCAP) for financial support, the Franco-Brazilian Scientific Collaboration Framework (CAPES-COFECUB) for continuous support (projects 869/15 and 981/20), and the reviewers of RBGeomorfologia for their comments and suggestions that contributed to the final version of the manuscript.

Conflict of Interest: The authors declare that there is no conflict of interest.

References

1. AB'SÁBER, A. N. Participação das superfícies aplainadas nas paisagens do Nordeste brasileiro. **Boletim Geomorfologia**, n. 19, p. 1-38, 1969.
2. AITKEN M. J. **An Introduction to Optical Dating**. London: Oxford University Press, 1988. p. 267.
3. ALMEIDA, F. F. M.; HASUI, Y.; BRITO NEVES, B. B.; FUCK, R. A. Brazilian structural provinces: an introduction. **Earth-Science Reviews**, v. 17, n. 1-2, p. 1-29, 1981.
4. ALVARES, C. A.; STAPE, J. L.; SENTELHAS, P. C.; GONÇALVES, J. L. M.; SPAROVEK, G. Köppen's climate classification map for Brazil. **Meteorologische Zeitschrift**, v. 22, n. 6, p 711–728, 2013. DOI: 10.1127/0941-2948/2013/0507

5. ANGELIM, L. A. A.; MEDEIROS, V. C.; NESI, J. R.; TORRES, H. H. F.; SANTOS, C. A.; VEIGA JUNIOR, J. P.; MENDES, V. A. Programa Geologia do Brasil. **Geologia e recursos minerais do Estado do Rio Grande do Norte**. Escala 1.500.000. Recife: CPRM, 2006.
6. ARNOLD, M; MERCHEL, S; BOURLES, D. L; BRAUCHER, R; BENEDETTI, L; FINKEL, R. C; AUMAITRE, G; GOTTDANG, A; KLEIN, M. "**The French accelerator mass spectrometry facility ASTER: Improved performance and developments**". Nuclear Instruments and Methods in Physics Research B 268. 2010.
7. AULER, A. S., SMART, P. L. Late Quaternary paleoclimate in semiarid northeastern Brazil from U-series dating of travertine and water-table speleothems. **Quat. Res**., v. 55, p. 159–167, 2001.
8. BASTOS, F. H.; CORDEIRO, A. M. C. Propriedades geomorfológicas das rochas e sus repercussões no relevo do Nordeste Setentrional do Brasil. **William Morris Davis - Revista de Geomorfologia**, v. 2, n. 1, p. 1-33, 2021. DOI: 10.48025/ISSN2675-6900.v2n1.2021.135
9. BALCO, G.; STONE, J.; LIFTON, N.; DUNAI, T. A complete and easily accessible means of calculating surface exposure ages or erosion rates from ^{10}Be and ^{26}Al measurements. **Quat. Geochronol**, v. 3, p. 174-195, 2008.
10. BELARMINO, Y; BASTOS, F. H. Análise Morfoestrutural e aplicação do Índice Declividade Extensão (RDE) na bacia hidrográfica do rio Ubatuba, divisa CE/PI, Nordeste do Brasil. **Revista Brasileira de Geomorfologia**, v. 22, n. 2, 2021. DOI: 10.20502/rbg.v22i2.1974.
11. BEHLING, H.; ARZ, H. W.; PÄTZOLD, J.; WEFER, G. Late Quaternary vegetational and climate dynamics in northeastern Brazil, inferences from marine core GeoB 3104-1. **Quaternary Science Reviews**, v. 19, n. 10, p. 981-994, 2000.
12. BEZERRA, F. H. R; VITA-FINZI, C. How active is a passive margin? Paleoseismicity in Northeastern Brasil. **Geology**, v. 28, p. 591–594, 2000.
13. BEZERRA, F. H. R.; NEVES, B. B. B.; CORREA, A. C. B.; BARRETO, A. M. F.; SUGUIO, K. Late Pleistocene tectonic geomorphological development within a passive margin—the Cariatá trough, northeastern Brazil. **Geomorphology**, v. 01, p. 555–582, 2008.
14. BÉTARD, F.; PEULVAST, J. P. Evolução morfoestrutural e morfopedológica do Maciço de Baturité e de seu piemont: do cretáceo ao presente. In: BASTOS, F. H. (Org.). **Serra de Baturité**: uma visão integrada das questões ambientais. Fortaleza: Expressão Gráfica, 2011. p. 35-59.
15. BIGARELLA, J. J.; ANDRADE, G. O. **Considerações sobre a estratigrafia dos sedimentos cenozoicos em Pernambuco (Grupo Barreiras)**. UR – ICT. Arquivos, 2. Recife. 1964.
16. BIERMAN, P. R.; CAFFEE, M. W. Slow rates of rock surface erosion and sediment production across the Namib Desert and escarpment, Southern Africa. **American Journal of Science**, v. 301, p. 326-358, 2001. DOI: 10.2475/ajs.301.4-5.326.
17. BIERMAN, P.; STEIG, E. Estimating rates of denudation using cosmogenic isotope abundances in sediment. **Earth Surf. Process. Landf.**, v.21, 125e139, 1996.
18. BIERMAN, P. R.; NICHOLS, K. K.; MATMON, A.; ENZEL, Y.; LARSEN, J.; FINKEL, R. 10-Be shows that Namibian drainage basins are slowly, steadily and uniformly eroding. **Quaternary International**, v. 33, p. 167-168, 2007.
19. BIGARELLA, J. J.; ANDRADE, G. O. Considerações sobre a estratigrafia dos sedimentos cenozoicos em Pernambuco (Grupo Barreiras). **Instituto de Ciências da Terra**, n. 2, p. 1-14, 1964.
20. BORCHERS, B.; MARRERO, S.; BALCO, G.; CAFFEE, M.; GOEHRING, B.; LIFTON, N. Geological calibration of spallation production rates in the CRONUS-Earth project. **Quaternary Geochronology**, v. 31, p. 188–198, 2016.
21. BRAUCHER, R.; MERCHEL, S.; BORGOMANO, J.; BOURLÈS, D. L. Production of cosmogenic radionuclides at great depth: A multi element approach. **Earth and Planetary Science Letters**, v. 309, n. 1-2, p. 1-9, 2011.
22. BRITO NEVES, B. B.; FUCK, R. A.; PIMENTEL, M. M. The Brasiliano collage in South America: a review. **Brazilian Journal of Geology**, v. 03, n. 33, p. 493-518, 2016.
23. BROWN, E.; STALLARD, R.; LARSEN, M.; RAISBECK, G.; YIOU, F. Denudation rates determined from the accumulation of in situ-produced 10Be in the Luquillo Experimental Forest, Puerto Rico. **Earth Planet. Sci. Lett**, v. 129, 193e202, 1995.
24. BRUNSDEN, D. The persistance of landforms. **Z. Geomorph, Suppl. Bd**., v. 93, p. 13–28. 1993.
25. BULL, W. B.; VAN DONK, J. Insolation chances, ice volumes and the 18O record of deep sea cores. **Rev. Geophys Space Phys**, v. 8, p. 169-197. 1970.
26. CASTRO, D. L.; BEZERRA, F. H. R. Fault Evolution in the Potiguar rift termination, equatorial margin of Brazil. **Solid Earth**, v. 6, p. 185–196, 2015.
27. CASTRO, D. L.; CASTELO BRANCO, R. M. G. "Caracterização da arquitetura interna das bacias do Vale do Cariri (NE do Brasil) com base em modelagem gravimétrica 3-D". **Revista Brasileira de Geofísica**, v. 17, n. 2-3, p. 129-144, 1999.
28. CAVALCANTE, J.C. **Limites e evolução geodinâmica do Sistema Jaguaribeano, Província Borborema, Nordeste do Brasil**. Dissertação (Mestrado em Geodinâmica) - Programa de Pós-Graduação em Geodinâmica e Geofísica, Universidade Federal do Rio Grande do Norte, Natal, 1999. 177p.

29. CEARÁ. **Perfil Básico Municipal**. Instituto de Pesquisa e Estratégia Econômica do Ceará. 2017. https://www.ipece.ce.gov.br/perfil-municipal-2017/.
30. CHEREM, L. F. S.; VARAJÃO, C. A. C.; BRAUCHER, R.; BOURLÉS, D.; SALGADO, A. A. R.; VARAJÃO, A. C. Long term Evolution of denudational escarpments in southeastern Brazil. **Geomorphology**, v. 173-174, p. 118-127, 2012. DOI: 10.1016/j.geomorph.2012.06.002.
31. CHMELEFF, J.; VON BLANCKENBURG, F.; KOSSERT, K.; JAKOB, D. Determination of the ^{10}Be half-life by multicollector ICP-MS and liquid scintillation counting. Nucl. Instrum. Methods Phys. **Res. B. Beam Interact. Mater. At**., v. 268, 192e199, 2010.
32. CODILEAN, A. T.; MUNACK, H.; COHEN, T. J.; SAKTURA, W.; GRAY, A. G.; MUDD, S. M. Octopus: an open cosmogenic isotope and luminescence database. **Earth System Science Data Discussions**, v. 10, n. 4, p. 1–23. 2018. DOI: 10.5194/essd-10-2123-2018.
33. CODILEAN, A. T.; MUNACK, H.; SAKTURA, W. M.; COHEN, T. J.; JACOBS, Z.; ULM, S.; HESSE, P. P.; HEYMAN, J.; PETERS, K. J.; WILLIAMS, A. N.; SAKTURA, R. B. K.; RUI, X.; CHISHIRO-DENNELLY, K.; PANTA, A. Octopus database. v. 2. **Earth System Science Data**, v. 14, n. 8, 3695-3713, 2022.
34. CORBETT, L. B.; BIERMAN, P. R.; ROOD, D. H. An approach for optimizing in situ cosmogenic ^{10}Be sample preparation. **Quaternary Geochronology**, v. 33, p 24-34. 2016
35. CORDEIRO, A. M. N. **Morfoestrutura e morfopedologia da Serra do Quincuncá e entorno, CE – Brasil**. Tese (Doutorado em Geografia) – Programa de Pós-Graduação em Geografia, Universidade Estadual do Ceará, Fortaleza, 2017. 252p.
36. CORDEIRO, A. M. N.; BASTOS, F. H.; MAIA, R. P. Formações concrecionárias e aspectos genéticos e evolutivos do maciço do Quincuncá, Província Borborema, Nordeste do Brasil. **Revista Brasileira de Geomorfologia**, v. 19, n. 2, p. 359-372, 2018. DOI: 10.20502/rbg.v19i2.1330.
37. CORREA, A. C. B.; TAVARES, B. A. C.; MONTEIRO, K. A.; CAVALCANTI, L. C. S; LIRA, D. R. Megageomorfologia e Morfoestrutura do Planalto da Borborema. Revista do Instituto Geológico, São Paulo, 2010.
38. COUTO, E. V.; SANTOS, L. J. C.; SORDI, V.; BOURLÉS, D.; BRAUCHER, R.; SALGADO, A. A. R.; LÉANNI, L.; FERREIRA, J. H. D. Changes in the base levels in the Ivaí and Paraná rivers confluence zone (southern Brazil): denudational reflexes in the evolution of the upRiver drainage network. **Zeitschrift fur Geomorphologie**, v. 62, n. 1, p. 23-40, 2018.
39. COX, R.; BIERMAN, P.; JUNGERS, M. C.; RAKOTONDRAZAFY, A. F. M. Erosion rates and sediment sources in Madagascar inferred from ^{10}Be analysis of lavaka, slope, and river sediment. **The Journal of Geology**, v. 117, n. 4, p. 363-376, 2009.
40. CPRM. Serviço Geológico do Brasil. **Mapa Geológico do Estado do Ceará**. Escala 1:500.000, Ceará. CPRM, 2020.
41. DEMANGEOT, J. Essair sur le relief du Nord-est Brésilien. **Ann. de Geographie**, v. 69, n. 372, p. 157-176, 1960.
42. DRESCH, J. Les problèmes géomorphologiques du Nord-Est Brésilien. **Bulletin de l'Association de Géographes Français**, v. 34, n. 263-264, p. 48-59, 1957.
43. DRUMOND, M. A.; BARROS, N. F.; SILVA, A. F.; MEIRA NETO, J. A. A. Alterações fitossociológicas e edáficas da mata atlântica em função das modificações da cobertura vegetal. **Revista Árvore**, v. 20, n. 4, p. 451-466, 1996.
44. DUNNE, J.; ELMORE, D.; MUZIKAR, P. Scaling factors for the rates of production of cosmogenic nuclides for geometric shielding and attenuation at depth on sloped surfaces. **Geomorphology**, v. 27, n. 1-2, p. 3-11. 1999.
45. DUXBURY, J.; BIERMAN, P. R.; PORTENGA, E. W.; PAVICH, M. J.; SOUTHWORTH, S.; FREEMAN, S. P. H. T. Erosion rates in and around Shenandoah National Park, Virginia, determined using analysis of cosmogenic ^{10}Be. **American Journal of Science**, v. 315, p. 46-76, 2015. DOI: 10.2475/01.2015.02.
46. ETCHEBEHERE, M. L. C.; SAAD, A. R.; SANTONI, G. C.; CASADO, F. C.; FULFARO, V. J. Detecção de prováveis deformações neotectônicas no vale do Rio do Peixe, região ocidental paulista mediante aplicação de índices RDE (Relação Declividade-Extensão) em segmentos de drenagem. **Revista de Geociências**, v. 25, p. 271-289, 2006.
47. FRANÇOLIN, J. B. L.; SZATMARI, P. Mecanismo de rifteamento da porção oriental da margem norte Brasileira. **Revista Brasileira de Geociências**, v. 17, n. 2, p. 196–207, 1987.
48. GALBRAITH, R. F.; ROBERTS, R. G.; LASLETT, G. M.; YOSHIDA, H.; OLLEY, J. M. **Archaeometry**, v. 41, n. 2, p. 339-364, 1999.
49. GALBRAITH, R.F.; GREEN, P., Int. J. Rad. **App. And Instrumentation, Part D. Nuclear Tracks and Radiation Measurements** vol. 17, 197-206, 1990.
50. GOMES, J. R. C; VASCONCELOS, A. M. **Jaguaribe SW: folha SB.24-Y.** Estados do Ceará, Pernambuco e do Piauí. Rio de Janeiro: CPRM, 2000. Programa Levantamentos Geológicos Básicos do Brasil – PLGB, 2000.
51. GONZALEZ, V. S.; BIERMAN, P. R.; FERNANDES, N.; ROOD, D. H. Long term background denudation rates of southern and southeastern Brazilian watersheds estimated with cosmogenic ^{10}Be. **Geomorphology,** v. 268., p. 54-63, 2016.

52. GOUVEIA SOUZA, C. R. The Bertioga coastal plain: an example of morphotectonic evolution. In: VIEIRA, B.; SALGADO, A.; SANTOS, L. (Eds.). Landscapes and landforms of Brazil. World Geomorphological Landscapes. Springer, Dordrecht. 2015.
53. GRANGER, D. E.; SCHALLER, M. Cosmogenic nuclides and erosion at the watershed scale. **Elements**, v. 10, n. 5, p. 369-373, 2014.
54. GRANGER, D. E.; KIRCHNER, J. W.; FINKEL, R. Spatially averaged long-term erosion rates measured from in situ-produced cosmogenic nuclides in alluvial sediment. **The Journal of Geology**, v. 104, n. 3, p. 249-257, 1996.
55. GRANGER, D. E.; LIFTON, N. A.; WILLENBRING, J. K. A cosmic trip: 25 years of cosmogenic nuclides in geology. **GSA Bulletin**, v. 125, n. 9-10, p. 1379-1402, 2013.
56. GUÉRIN, G., MERCIER, N., NATHAN, R. and ADAMIEC, G., **Radiation Measurements**, vol. 47, 778-785, 2012.
57. GURGEL, S. P. P. **Evolução morfotectônica do maciço estrutural do Pereiro, Província Borborema**. Tese (Doutorado em Geodinâmica) - Programa de Pós-Graduação em Geodinâmica e Geofísica, Universidade Federal do Rio Grande do Norte, Natal, 2012. 189p.
58. GURGEL, S. P. P.; BEZERRA, F. H. R.; CORRÊA, A. C. B.; MARQUES, F. O.; MAIA, R. P. Cenozoic uplift and erosion of structural landforms in NE Brazil. **Geomorpholog**y, v. 186, p. 68-84, 2013.
59. HACK, J. T. River-profile analysis and River-gradient index. Journal of Research of the U. S. **Geological Survey**, v. 1, n.4, p. 421-429, 1973.
60. HARRIS, S. E.; MIX, A. C. Climate and tectonic influences on continental erosion of tropical South America, 0-13 Ma. **Geology**, v. 30, n. 5, p. 447–450, 2002.
61. HAWKER, L.; UHE, P.; PAULO, L.; SOSA, J.; SAVAGE, J.; SAMPSON, C.; NEAL, J. A 30 m global map of elevation with forests and buildings removed. **Environmental Research Lett**, v. 17, 024016, 2022. DOI: 10.1088/1748-9326/ac4d4f.
62. HEIMSATH, A. M.; CHAPPEL, J.; FINKEL, R. C.; FIFIELD, K.; ALIMANOVIC, A. Escarpment erosion and landscape evolution in southeastern Australia. In: WILLETT, S. D.; HOVIUS, N.; BRANDON, M. T.; FISHER, D. M. (Eds.). **Tectonics, climate, and landscape evolution. Geological Society of America,** Special Paper, v. 398, 2006. p. 173–190.
63. HUNTLEY, D. J.; CLAGUE, J. J. Optical dating of tsunami-laid sands. **Quaternary Research**, v. 46, p. 127–140. 1996.
64. HUNTLEY, D. J.; GODFREY-SMITH, D. I.; THEWALT, M. L. W. Optical dating of sediments. **Nature**, v. 313, p. 105–107. 1985.
65. JELINEK, A. R.; CHEMALE Jr., F.; VAN DER BEEK, P. A. GUADAGNIN, F.; CUPERTINO, J. A.; VIANA, A. Denudation history and landscape evolution of the northern East Brazilian continental margin from apatite fission-track thermochronology. **J. S. Am. Earth Sci**., v. 54, p. 158–181, 2014.
66. JELINEK, A. R.; CORRÊA-GOMES, L. C.; BICCA, M. M. Evolução termotectonica fanerozoica da margem continental na área do Rifte Reconcavo-Tucano-Jatobá. **Pesquisa em Geociências**, v. 47, n. 1, e0823, 2020. DOI: 10.22456/1807-9806.101330.
67. KIRBY, E., WHIPPLE, K. X., Expression of active tectonics in erosional landscapes**. Journal of structural geology** 44, 54-75. https://doi.org/10.1016/j.jsg.2012.07.009. 2012.
68. KORSCHINEK, G.; BERGMAIER, A.; FAESTERMANN, T.; GERSTMANN, U.; KNIE, K.; RUGEL, G.; WALLNER, A.; DILLMANN, I.; DOLLINGER, G.; LIERSE VON GOSTOMSKI, C.; KOSSERT, K.; MAITI, M.; POUTIVTSEV, M.; REMMERT, A. A new value for the half-life of 10Be by heavy-ion elastic recoil detection and liquid scintillation counting. Nucl. Instrum. Methods Phys. **Res. B Beam Interact. Mater. At.**, v. 268, 187e191, 2010.
69. LIMA, M. G. **A história do intemperismo na Província Borborema Oriental, Nordeste do Brasil: implicações climáticas e tectônicas**. Tese (Doutorado em Geodinâmica) – Programa de Pós-Graduação em Geodinâmica e Geofísica, Universidade Federal do Rio Grande do Norte, Natal, 2008. 255p.
70. LIMA, K. C.; PEREZ FILHO, A. Geomorphological evolution of the coastal plains in the Holocene. **Mercator**, v. 19, e19010, 2020.
71. LINARI, C. J.; BIERMAN, P. R.; PORTENGA, E. W.; MILAN J. P.; FINKEL, R. C. Rates of erosion and landscape change along the Blue Ridge escarpment, southern Appalachian Mountains, estimated from in situ cosmogenic ^{10}Be. **Earth Surfaces Processes and Landform**, v.42, n. 6, p. 928-940, 2017.
72. LISTO, D. G. S.; BALDER, R. F. T. M.; CORRÊA, A. C. B.; RAMOS, D. A. M. C.; CALEGARI, M. R. Weathering pits as a geochronometer of environmental changes in the State of Pernambuco, Northeastern Brazil. **Quaternary International**, v. 649, p. 58-71, 2023. DOI: 10.1016/j.quaint.2022.10.004.
73. MAIA, R. P.; BEZERRA, F. H. R. **Structural Geomorphology in Northeastern Brazil**. Springer Briefs in Latin American Studies, 2020.
74. MAIA, R. P.; NASCIMENTO, M. A. L. Relevos graníticos do Nordeste brasileiro. **Revista Brasileira de Geomorfologia**, v. 19, n. 2, p. 373-389. DOI: 10.20502/rbg.v19i2.1295 2018.

75. MATMON, A.; BIERMAN, P. R.; LARSEN, J.; SOUTHWORTH, C. S.; PAVICH, M. J.; FINKEL, R. C.; CAFFEE, M. W. Erosion of an ancient mountain range, the Great Smoky Mountains, North Carolina and Tennessee. **American Journal of Science**, v. 303, p. 817-855. DOI: 10.2475/ajs.303.9.817. 2003.
76. MATOS, R. C. D. The Northeast Brazilian rift system. **Tectonics**, v. 11, n. 4, p. 766-791, 1992.
77. MATOS, R. C. D. Tectonic evolution of the equatorial South Atlantic. In: MOHRIAK, W; TALWANI, M. (Eds.). **Atlantic rift and continental margin**. American Geophysical Union. Publisher Am. Geophys. Union, Washington D. C. 2000. p. 331-354.
78. MCMURRY, J.; LEON E. L.; ALCIDES N. S. Evolution of a heterogeneous, continentally derived granite: Dona Inês Pluton, Northeastern Brazil. **The Journal of Geology**, v. 95, n. 1, p. 107-117, 2015. DOI: 10.1086/629109.
79. MORAIS NETO, J. M.; HEGARTY, K.; KARNER, G.D. Abordagem preliminar sobre paleotemperatura e evolução do relevo da bacia do Araripe, Nordeste do Brasil, a partir da análise de traços de fissão em apatita. **Boletim de Geociências da Petrobrás**, v. 14, n. 1, p. 113-119, 2005.
80. MURRAY, A. S.; WINTLE, A. G. Luminescence dating of quartz using an improved single aliquot regenerative-dose protocol. **Radiation Measurements**, v. 32, p. 57-73, 2000. DOI: 10.1016/S1350-4487(99)00253-X 2000.
81. NASCIMENTO, M. A. L.; MEDEIROS, V. C.; GALINDO, A. C. Ediacaran to Cambrian magmatic suites in the Rio Grande do Norte domain, extreme Northeastern Borborema Province (NE of Brazil): current knowledge. **Journal of South American Earth Sciences**, v. 58, p. 281-299, 2015.
82. NISHIIZUMI, K.; IMAMURA, M.; CAFFEE, M.; SOUTHON, J.; FINKEL, R.; MCANINCH, J. Absolute calibration of ^{10}Be AMS standards. Nucl. Instrum. Methods Phys. **Res. B Beam Interact. Mater. At.**, v. 258, 403e413, 2007.
83. NOGUEIRA, F. C.; BEZERRA, F. H. R.; FUCK, R. A. Quaternary fault kinematics and chronology in intraplate Northeastern Brazil. **Journal of Geodynamics**, v. 49, n. 2, p. 79–91, 2010. DOI: 10.1016/j.jog.2009.11.002.
84. O'LEARY, Dennis W.; FRIEDMAN, Jules Daolun; POHN, Howard A. Lineament, linear, lineation: some proposed new standards for old terms. **Geological Society of America Bulletin**, v. 87, p. 1463-1469, 1976.
85. PALUMBO, L.; HETZEL, R.; TAO, M.; LI, X. Catchment-wide denudation rates at margin of NE Tibet from in situ-produced cosmogenic ^{10}Be. **Terra Nova**, v. 23, p. 42-48, 2011.
86. PEIFER, D.; CREMON, É. H.; ALVES, F. C. Ferramentas modernas para a extração de métricas de gradientes fluviais a partir de MDEs: uma revisão. Revista Brasileira de Geomorfologia 21 (1), 117-138. DOI: 10.20502/www.ugb.org.br rbg.v21i1.1732. 2020.
87. PEYERL, W. R. L.; SALAMUNI, E.; QUEIROZ, G. L.; SILVA, C. L.; GARCIA, V. H. Identification of morphostructures by utilizing Knickpoint Ranks, a method to avoid the camouflage effect in knickpoint analysis. **Geomorphology,** v. 442, 2023.
88. PETIT, J. R.; JOUZEL, J.; RAYNAUD, D.; BARKOV, N. I.; BARNOLA, J. M.; BASILE, I.; BENDER, M.; CHAPPELLAZ, J.; DAVIS, M.; DELAYGUE, G.; DELMOTTE, M.; KOTLYAKOV, V. M.; LEGRAND, M.; LIPENKOV, V. Y.; LORIUS, C.; PÉPIN, L.; RITZ, C.; SALTZMAN, E.; STIEVENARD, M. Climate and atmospheric history of the past 420,000 years from the Vostok ice core, Antartica. **Nature**, v. 399, p. 429-36. 1999.
89. PEULVAST, J. P.; BETARD, F. Late Cenozoic and present-day hillslope erosion dynamics in a passive margin context: stability or instability? Case studies in Northeast Brazil. **Geografia Fisica e Dinamica Quaternaria**, v. 36, p. 139–49, 2013. DOI: 10.4461/GFDQ.2013.36.11. 2013.
90. PEULVAST, J. P.; BETARD, F. Morphostratigraphic constraints and low temperature thermochronology: Lessons from a review of recent geological and geomorphological studies in northeast Brazil. **Journal of South American Earth Sciences**, v. 111, 2021. DOI: 10.1016/j.jsames.2021.103464.
91. PEULVAST, J. P.; BETARD, F.; LAGEAT, Y. Long-term landscape evolution and denudation rates in basement and platform areas: the contribution of the morphostratigraphic approach. **Geomorphol. Relief, Process. Environ**., v. 2, p. 95–108. 2009.
92. PEULVAST, J. P.; CLAUDINO-SALES, V. Stepped surfaces and palaeolandforms in the northern Brazilian <<Nordeste>>: constraints on models of morphotectonic evolution. **Geomorphology**, v. 62, p. 89-122, 2004.
93. PEULVAST, J. P.; CLAUDINO SALES, V.; BEZERRA, F. H.; BETARD, F. Landforms and neotectonics in the equatorial passive margin of Brazil. **Geodinamica Acta**, v. 9, n. 1, p. 51–71. 2006. DOI: 10.3166/ga.19.51-71. 2006.
94. PINÉO, T. R. G.; PALHETA, E. S. M.; COSTAS, F. G.; VASCONCELOS, A. M.; GOMES, F. E. M.; BESSA, M. D. M. R.; LIMA, A. F.; HOLANDA, J. L. R.; FREIRE, D. P. C. **Mapa de Recursos Minerais do Estado do Ceará**. Escala de 1:500.00. Fortaleza: CPRM, 2020.
95. PORTENGA, E.; BIERMAN, P. Understanding Earth's eroding surface with ^{10}Be. **GSA Today**, v. 21, 4e10, 2011.
96. PORTENGA, E., BIERMAN, P., DUNCAN, C., CORBETT, L.B., KEHRWALD, N.M, ROOD, D.H. Erosion rates of the Bhutanese Himalaya determined using in situ-produced ^{10}Be. **Geomorphology**, v. 233, p. 112-126, 2015.

97. PRESCOTT, J. R.; HUTTON, J. T. Cosmic Ray Contributions to Dose-Rates for Luminescence and ESR Dating: Large Depths and Long Terms Time Variations. Radiation Measurements, vol.23, 497-500, 1994.
98. REZENDE, E. A.; SALGADO, A. A. R.; SILVA, J. R.; BOURLÉS, D.; LEÁNNI, L. Factores controladores da evolução do relevo no flanco NNW do rift continental do sudeste do Brasil: uma análise baseada na mensuração dos processos denudacionais de longo-termo. **Revista Brasileira de Geomorfologia**, v. 1, n. 2, p. 221-234, 2013.
99. QUIGLEY, M.; SAFIFORD, M.; FIFIELD, K.; ALIMANOVIC, A. Bedrock erosion and relief production in the northern Flinders Ranges, Australia. **Earth Surface Processes and Landforms**, v. 32, p. 929-944, 2007.
100. ROCCA, R. R.; TATUMI, S.; WATANABE, S.; ROSSETI, D. F. OSL Dating of Coastal Post-Barreiras Sediments from Northern Brazil. **Journal of Earth Science and Engineering**, v. 2, p. 515-521, 2012.
101. ROSSI, M. W.; QUINGLEY, M. C.; FLETCHER, J. M.; WHIPPLE, K. X.; DIAZ TORRES, J. J.; SEILER, C.; FIFIELD, L. K.; HEIMSATH, A. M. Along strike variation in catchment morphology and cosmogenic denudation rates reveal the patter and history of footwall uplift, Main Gulf Escarpment, Baja California. **GSA Bulletin**, v. 129, n. 7-8, p. 837-854, 2017. DOI: 10.1130/B31373.1.
102. ROSSETTI, D. F. Paleosurfaces from Northeastern Amazonia as a Key for reconstructing paleolandscapes and understanding weathering products. **Sedimentary Geology**, v. 169, n. 3, p. 151–74, 2004. DOI: 10.1016/j.sedgeo.2004.05.003.
103. SAADI, A.; BEZERRA, F. H. R.; COSTA, R. D.; IGREJA, H. L. S.; FRANZINELLI, E. Neotectônica da plataforma brasileira. In: Souza, C. R. G. (Ed.). **Quaternário do Brasil**. Ribeirão Preto: Holos Editora, 2005. p. 211-234.
104. SALGADO, A. A. R.; MARENT, B. R.; CHEREM, L. F. S.; BOURLÈS, D.; SANTOS, L. J. C.; BRAUCHER, R.; BARRETO, H. N. Denudation and retreat of the Serra do Mar escarpment in Southern Brazil derived from in situ-produced ^{10}Be concentration in river sediment. **Earth Surface Processes and Landforms,** v. 39, p. 311-319, 2014.
105. SALLUN, A. E. M.; SUGUIO, K.; TATUMI, S. H.; YEE, M.; SANTOS, J.; BARRETO, A. M. F. Datação absoluta de depósitos quaternários brasileiros por luminescência. **Revista Brasileira de Geociências**, v. 37, n. 2, p. 402-413, 2007.
106. SALLUM, A. E. M.; SUGUIO, K. Quaternary colluvial episodes (Upper Paraná River Hydrographic Basin, BR). **Academia Brasileira de Ciências**, v. 82, n. 3, p. 701-715, 2010.
107. SAWAKUCHI, A. O.; MENDES, V. R.; PUPIM, F. N.; MINELI, T. D.; RIBEIRO, L. M. A. L.; ZULAR, A.; GUEDES, C. C. F.; GIANNINI, P. C. F.; NOGUEIRA, L.; FILHO, W. S.; ASSINE, M. L. Optically stimulated luminescence and isothermal thermoluminescence dating of high sensitivity and well bleached quartz from Brazilian sediments: from Late Holocene to beyond the Quaternary? **Brazilian Journal of Geology**, v. 46, n. l 1, p. 209-226, 2016.
108. SCHWANGHART, W., SCHERLER, D. TopoToolbox 2–MATLAB-based software for topographic analysis and modeling in Earth surface sciences. **Earth Surface Dynamics**, v. 2, n. 1, p.1-7, 2014. https://doi.org/10.5194/esurf-2-1-2014.
109. SCHWANGHART, W., SCHERLER, D., Bumps in river profiles: uncertainty assessment and smoothing using quantile regression techniques. **Earth Surface Dynamics**, v. 5, n. 4, p. 821-839, 2017. https://doi.org/10.5194/esurf-5-821-2017.
110. SILVA, R. N.; GOMES, D. D. M.; LIMA, C. E. S.; GOLDFARB, M. C. Uso do índice RDE para determinação de anomalias de drenagem no Rio Capibaribe (PE). **REGET/UFSM**, v. 20, n. 1, p. 552-565, 2006.
111. SILVERMAN, B.W., **Density Estimation for Statistics and Data Analysis**. Routledge. 1998.
112. SORDI, M. V.; SALGADO, A. A. R.; SIAME, L.; BOURLÊS, D.; PAISANI, J. C.; LÉANNI, L.; BRAUCHER, R.; COUTO, E. V. Implications of drainage rearrangement for passive margin escarpment evolution in southern Brazil. **Geomorphology**, v. 306, p. 155-169, 2018.
113. STONE, J. O. Air pressure and cosmogenic isotope production. **Journal of Geophysical Research**, v. 105, n. 10, p. 23753–23759, 2000.
114. TEODORO, V. L. I.; TEIXEIRA, D.; COSTA, D. J. L.; FULLER, B. B. O conceito de bacia hidrográfica e a importância da caracterização morfométrica para o entendimento da dinâmica ambiental local. **Revista Uniara**, n. 20, p. 137-157, 2007.
115. TUCCI, C. E. M. Escoamento Superficial. In: TUCCI, C. E. M. (Org.). **Hidrologia**: ciência e aplicação. 2. ed. Porto Alegre: Ed. Universidade/UFRGS: ABRH, 2000. p. 391-441.
116. TUDELA, D. R. G.; MITTANI, J. C. R.; TATUMI, S. H.; ROSSETI, D. F.; MUNITA, C. S. **OLS dating results of post barreiras sediments in the Paraíba Basin, Northeastern Brazil**. International Nuclear Atlantic Conference – INAC. 2011.
117. UTIDA, G.; CRUZ, F. W.; SANTOS, R. V.; SAWAKUCHI, A. O.; WANG, H.; PESSENDA, L. C. R.; NOVELLO, V. F.; VUILLE, M.; STRAUSS, A. M; BORELLA, A. C.; STRÍKIS, N. M.; GUEDES, C. C.; DE ANDRADE, F. R. D.; ZHANG, H.; CHENG, H.; EDWARDS, R. L. Climate changes in Northeastern Brazil from deglacial to Meghalayan periods and related environmental impacts. Quaternary Science Reviews, 250, 106655, 2020, DOI: 10.1016/j.quascirev.2020.106655
118. VENANCIO, I. M.; SHIMIZU, M. H.; SANTOS, T. P.; LESSA, D. O.; DIAS, B. B.; CHIESSI, C. M.; MULITZA, S.; KUHNERT, H.; TIEDEMANN, R.; VAHLENKAMP, M.; BICKERT, T.; BELEM, A. L; SAMPAIO, G.; ALBUQUERQUE, A. L. S.; NOBRE,

C. Ocean-atmosphere interactions over the western South Atlantic during Heinrich stadials. **Global and Planetary Change**, v. 195, 103352, 2020. DOI: 10.1016/j.gloplacha.2020.103352.

119. VON BLANCKENBURG, F. The control mechanisms of erosion and weathering at basin scale from cosmogenic nuclides in river sediment. **Earth Planet. Sci. Lett.**, v. 237, p. 462-479, 2005.
120. VON BLANCKENBURG, F.; WILLENBRING, J. Cosmogenic nuclides: dates and rates of earth-surface change. **Elements**, v. 10, n. 5, p. 341-346, 2014.
121. WALLINGA, J.; MURRAY, A.; WINTLE, A. The single-aliquot regenerative dose (SAR) protocol applied to coarse-grain feldspar. **Radiation Measurements**, v. 32, n. 5–6, p. 529-533, 2000. DOI: 10.1016/S1350-4487(00)00091-3.
122. WALKER, M. J. C. **Quaternary dating methods**. John Wiley & Wiley. 2005. 304p.
123. WANG, X.; AULER, A. S.; EDWARDS, R. L.; CHENG, H.; CRISTALLI, P. S.; SMART, P. L.; RICHARDS, D. A.; SHEN, C. C. Wet periods in northeastern Brazil over the past 210 kyr linked to distant climate anomalies. **Nature**, v. 432, p. 740-743, 2004.
124. WELLS, S. G.; MCFADDEN, L. D.; DOHRENWEND, J. C. Influence of late quaternary climatic changes on geomorphic and pedogenic processes on a desert piedmont, eastern Mojave Desert, California. **Quarternary Res.**, v. 27, p. 130-146, 1987.
125. WHIPPLE, K. X., FORTE, A. M., DIBIASE, R. A., GASPARINI, N. M., OUIMET, W. B., Timescales of landscape response to divide migration and drainage capture: Implications for the role of divide mobility in landscape evolution. Journal of Geophysical Research: Earth Surface, v. 122, n. 1, p. 248-273, 2017. DOI: 10.1002/2016JF003973.
126. WOBUS, C., WHIPPLE, K. X., KIRBY, E., SNYDER, N., JOHNSON, J., SPYROPOLOU, K., CROSBY, B., SHEEHAN, D., **Tectonics from topography: Procedures, promise, and pitfalls**. DOI:10.1130/2006.2398(04). 2006.
127. XIMENES NETO, A. R.; SILVA, R. R.; PAULA, D. P.; LEISNER, M. M.; CORDEIRO, A. M. N.; MORAIS, J. O.; PINHEIRO, L. S. Spatial distribution and deposits of cliffs along the Brazilian semi-arid coast. **Geomorpholog**y, v. 466, p. 1-19, 2024. DOI: 10.1016/j.geomorph.2024.109451.
128. ZHANG, Y.; CHIESSI, C. M.; MULITZA, S.; SAWAKUCHI, A. O.; HÄGGI, C.; ZABEL, M. Different Precipitation Patterns across Tropical South America during Heinrich and Dansgaard-Oeschger Stadials. **Quat. Sci. Rev**., v. 177, p. 1–9, 2017. DOI: 10.1016/j.quascirev.2017.10.012.